Monthly Notices of the ROYAL ASTRONOMICAL SOCIETY

MNRAS **445,** 1430–1448 (2014) doi:10.1093/mnras/stu1745

The largest X-ray-selected sample of $z > 3$ AGNs: C-COSMOS and ChaMP

E. Kalfountzou,[1,2]★ F. Civano,[1,3] M. Elvis,[1] M. Trichas[4] and P. Green[1]

[1]*Harvard–Smithsonian Center for Astrophysics, 60 Garden St, Cambridge, MA 02138, USA*
[2]*Centre for Astrophysics, Science & Technology Research Institute, University of Hertfordshire, Hatfield, Herts AL10 9AB, UK*
[3]*Yale Center for Astronomy and Astrophysics, 260 Whitney Ave, New Haven, CT 06520-8121, USA*
[4]*Airbus Defence & Space, Gunnels Wood Road, Stevenage, Hertfordshire SG1 2AS, UK*

Accepted 2014 August 25. Received 2014 August 22; in original form 2014 May 29

ABSTRACT

We present results from an analysis of the largest high-redshift ($z > 3$) X-ray-selected active galactic nucleus (AGN) sample to date, combining the *Chandra* Cosmological Evolution Survey and *Chandra* Multi-wavelength Project surveys and doubling the previous samples. The sample comprises 209 X-ray-detected AGNs, over a wide range of rest-frame 2–10 keV luminosities $\log L_{\rm X} = 43.3$–$46.0\,{\rm erg\,s^{-1}}$. X-ray hardness rates show that ∼39 per cent of the sources are highly obscured, $N_{\rm H} > 10^{22}\,{\rm cm^{-2}}$, in agreement with the ∼37 per cent of type-2 AGNs found in our sample based on their optical classification. For ∼26 per cent of objects have mismatched optical and X-ray classifications. Utilizing the $1/V_{\rm max}$ method, we confirm that the comoving space density of all luminosity ranges of AGNs decreases with redshift above $z > 3$ and up to $z \sim 7$. With a significant sample of AGNs ($N = 27$) at $z > 4$, it is found that both source number counts in the 0.5–2 keV band and comoving space density are consistent with the expectation of a luminosity-dependent density evolution (LDDE) model at all redshifts, while they exclude the luminosity and density evolution (LADE) model. The measured comoving space density of type-1 and type-2 AGNs shows a constant ratio between the two types at $z > 3$. Our results for both AGN types at these redshifts are consistent with the expectations of LDDE model.

Key words: surveys – galaxies: active – X-rays: galaxies.

1 INTRODUCTION

Active galactic nucleus (AGN) evolution at high redshifts, before their density peak, illuminates the role of AGN in the formation and co-evolution of galaxies and their central supermassive black holes (SMBHs) during the time of rapid SMBH growth. The so-called downsizing evolution has been revealed for both AGN (e.g. Ueda et al. 2003; Hasinger, Miyaji & Schmidt 2005; Aird et al. 2010) and galaxies (e.g. Cowie et al. 1996; Kodama et al. 2004; Draper et al. 2009). Supporting this idea, X-ray surveys have shown that the number density of luminous AGN peaks at higher redshifts than less luminous ones (e.g. Ueda et al. 2003; Aird et al. 2010). This sort of cosmological co-evolution scenario is inferred from the tight correlation exists locally between SMBH mass and galactic bulge properties (e.g. Magorrian et al. 1998; Ferrarese & Merritt 2000; Gebhardt et al. 2000; McConnell & Ma 2013).

To elucidate the co-evolution of SMBH and galaxies (e.g. Granato et al. 2001, 2004; Croton et al. 2006; Hopkins et al. 2006; Menci et al. 2008; Trichas et al. 2009, 2010; Kalfountzou et al. 2011, 2012, 2014), the accretion activity in the Universe has to be studied both at high redshifts and for low luminosities. This requires large samples of AGNs spanning wide ranges of properties. While many optical surveys have investigated the space density of high-redshift AGNs (e.g. Richards et al. 2006; Jiang et al. 2009; Willott et al. 2010; Glikman et al. 2011; Ikeda et al. 2011; Ross et al. 2013), the results are still controversial due to their inevitable incompleteness, especially at the faint luminosity end due to the host contamination, and the bias against obscured sources. As compared with optical surveys, X-ray observations are less contaminated by the host galaxy emission and include AGN populations with a wide range of neutral hydrogen column density.

For the investigation of absorption evolution (e.g. Ueda et al. 2003; Hasinger 2008; Draper & Ballantyne 2010), X-ray selected samples include all types of AGN (e.g. type-1/unobscured and type-2/obscured) and provide reduced obscuration bias in comparison with optically selected AGN. Although X-ray surveys have inferred the existence of an anticorrelation between the obscured AGN fraction and the luminosity, several of these studies have suggested that this fraction increases toward higher redshift from $z = 0$ to $z \sim 2$ with limited samples at $z > 3$ (e.g. La Franca et al. 2005; Ballantyne, Everett & Murray 2006; Treister & Urry 2006; Ballantyne 2008; Hiroi et al. 2012).

★E-mail: el.kalfountzou@gmail.com

However, the evolution of AGN is still rife with uncertainty. On the basis of hard X-ray surveys, many studies agreed that the X-ray Luminosity Function (XLF) of AGN is best described by a luminosity-dependent density evolution (LDDE) model (e.g. Ueda et al. 2003; Gilli, Comastri & Hasinger 2007; Silverman et al. 2008; Ueda et al. 2014). Aird et al. (2010) preferred instead a luminosity and density evolution model (LADE). In LADE, the shift in the redshift peak of the AGN space density versus X-ray luminosity is much weaker than in LDDE models, yet gives a similarly good fit to their data. While the $z < 2$ downsizing behaviour is common to both models, quite different numbers of AGNs are predicted at higher redshifts ($z \geq 3$).

X-ray surveys (2–10 keV) are now sensitive enough to sample the bulk of the $z > 3$ AGN population. Two studies have been performed on high-redshift AGN exploiting the deep X-ray surveys in the Cosmological Evolution Survey (COSMOS) field carried out with *XMM–Newton* ($N_{\rm AGN} = 40$; Brusa et al. 2009) and *Chandra* ($N_{\rm AGN} = 81$; Civano et al. 2011), limited to 2–10 keV luminosities $L_{2-10\,\rm keV} > 10^{44.2}$ and $10^{43.5}\,\rm erg\,s^{-1}$, respectively. A more recent study based on the 4 Ms *Chandra* Deep Field South (CDF-S; Xue et al. 2011) was able to investigate the evolution of $z > 3$ AGN down to $L_{\rm X} \sim 10^{43}\,\rm erg\,s^{-1}$ ($N_{\rm AGN} = 34$; Vito et al. 2013). These results are consistent with a decline of the AGN space density at $z > 3$, but the shape of this decline remains highly uncertain at $z > 4$. To overcome these limitations, in this work we combined the two largest samples of $z > 3$ X-ray-selected AGNs with spectroscopic redshifts, both derived from *Chandra* X-ray Observatory (Weisskopf et al. 2002) surveys: the wide but shallow ChaMP survey (Kim et al. 2007; Green et al. 2009), and the deeper but narrower C-COSMOS survey (Elvis et al. 2009). This combination results in the largest X-ray AGN sample with $N_{\rm AGN} = 211$ at $z > 3$ and $N_{\rm AGN} = 27$ at $z > 4$. At the same time, by combining two surveys with different flux limits, we are able to determine the density evolution of both low-luminosity ($L_{\rm X} < 10^{44}\,\rm erg\,s^{-1}$) and high-luminosity AGNs. Our sample includes both obscured and unobscured AGNs, and their separate evolution has been determined.

The paper is structured as follows. In Section 2, we discuss the data sets used in this work and the selection of the high-z sample. In Section 3, we present the optical and X-ray properties of the selected high-z AGN sample, and we explain the AGN type classification using X-ray or optical data. In Sections 4 and 5, the number counts and space density of the sample are compared with model predictions. Section 6 summarizes the conclusions. A cosmological model with $\Omega_o = 0.3$, $\lambda_o = 0.7$, and a Hubble constant of $70\,\rm km\,s^{-1}\,Mpc^{-1}$ is used throughout (Spergel et al. 2003). Errors are quoted at the 1σ level.

2 SAMPLE SELECTION

The high-redshift AGN sample used in this work has been selected from the C-COSMOS X-ray catalogue, combining the spectroscopic and photometric information available from the identification catalogue of X-ray C-COSMOS sources (Civano et al. 2011, 2012) and the ChaMP (*Chandra* Multi-wavelength Project) X-ray catalogue using only the 323 ChaMP obsids overlapping with Sloan Digital Sky Survey (SDSS; Richards et al. 2006) DR5 imaging. In Fig. 1, we show the sky coverage (the area of a survey that is sensitive to sources above a given X-ray flux) using the observed soft band (0.5–2 keV) source detections for the two surveys, and their sum. This corresponds to 2–8 keV rest frame for $z > 3$.

A schematic diagram of the sample selection with the detailed number of sources for each step is presented in Fig. 2.

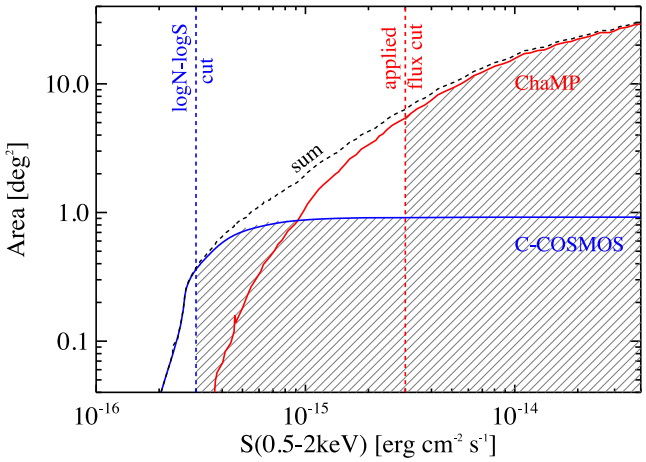

Figure 1. Sky area versus X-ray flux sensitivity curves for the C-COSMOS (blue solid line) and ChaMP/SDSS (red solid line) samples and the total area (black dashed line). The vertical blue dashed line indicates the flux corresponding to 10 per cent of the total C-COSMOS area (see Section 4). The vertical red dashed line indicates the ChaMP X-ray flux limit with >75 per cent completeness from SDSS/UKIDSS/*WISE* (see Section 2.2). The total area, after the applied cuts, used for this work is represented by the shadowed grey area.

2.1 The C-COSMOS sample

The *Chandra*-COSMOS survey (C-COSMOS; Elvis et al. 2009; Civano et al. 2012) covers the central 0.9 deg^2 of the COSMOS field up to a depth of 200 ks in the inner 0.5 deg^2, with the ACIS-I CCD imager (Garmire et al. 2003) on board *Chandra*. The C-COSMOS X-ray source catalogue comprises 1761 point-like X-ray sources detected down to a maximum likelihood threshold detml = 10.8 in at least one band. This likelihood threshold corresponds to a probability of $\sim 5 \times 10^{-5}$ that a catalogue source is instead a background fluctuation (Puccetti et al. 2009). Given this likelihood threshold, the flux limit reached in the survey is $5.7 \times 10^{-16}\,\rm erg\,cm^{-2}\,s^{-1}$ in the full band (0.5–10 keV), $1.9 \times 10^{-16}\,\rm erg\,cm^{-2}\,s^{-1}$ in the soft band (0.5–2 keV) and $7.3 \times 10^{-16}\,\rm erg\,cm^{-2}\,s^{-1}$ in the hard band (2–10 keV).

The $z > 3$ C-COSMOS sample, as presented by Civano et al. (2011), comprises 107 X-ray-detected sources with available spectroscopic (32) and photometric (45) redshifts plus 30 sources with a formal $z_{\rm phot} < 3$ but with a broad photometric redshift probability distribution, such that $z_{\rm phot} + 1\sigma_{\rm phot} > 3$. All of the spectroscopic C-COSMOS sources have a quality flag 3 (two sources) or four corresponding, respectively, to a secure redshift with two or more emission or absorption lines and a secure redshift with two or more emission or absorption lines with a good-quality, high S/N spectrum (see Lilly et al. 2007, 2009 for thorough explanation of quality flags). Tuned photometric redshifts for the C-COSMOS sources have been computed and presented in Salvato et al. (2011). Due to the large number of photometric bands and the sizeable spectroscopic training sample spanning a large range in redshift and luminosity the estimated photometric redshifts are expected to be quite robust at $z > 2.5$ even at the fainter magnitudes ($i_{AB} > 22.5$). The COSMOS photometric redshifts for X-ray-selected sources have an accuracy of $\sigma_{\Delta z/(1+z_{\rm spec})} = 0.015$ with a small fraction of outliers (<6 per cent), considering the sample as a whole at $i < 22.5$. At fainter magnitudes, the dispersion increases to $\sigma_{\Delta z/(1+z_{\rm spec})} = 0.035$ with ~15 per cent outliers, still remarkably good for an AGN sample. For the $z > 3$ C-COSMOS sample, an accuracy of $\sigma_{\Delta z/(1+z_{\rm spec})} = 0.014$ is

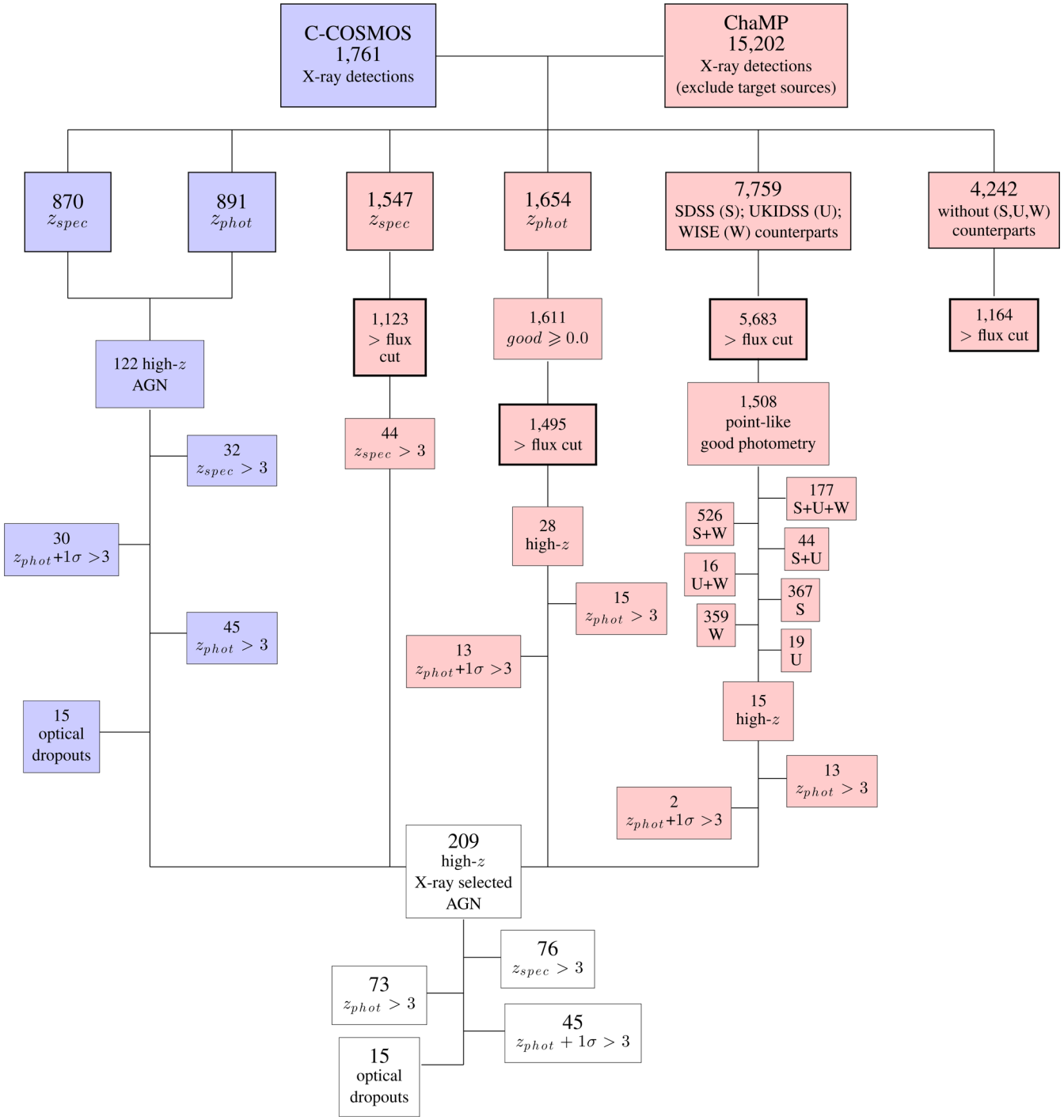

Figure 2. Schematic flow diagram of the high-z sample selection.

achieved with only three catastrophic outliers (<9 per cent). The spectral energy distributions (SEDs) of the sources with photometric redshift larger than 3 have been visually inspected together with the photometric fitting and the probability distribution of all the possible solutions.

There are 91 sources selected in the 0.5–2 keV band, 14 in the 2–10 keV, and 4 in the 0.5–10 keV bands. There are 15 C-COSMOS sources without a counterpart in the optical bands, but with a *K*-band and IRAC (7), only IRAC (6) or no infrared detection (2). Given the small number of bands in which these objects are detected, no photometric redshift is available for them. In X-ray-selected samples, non-detection in the optical band has been often assumed to be a proxy for high redshift (e.g. Koekemoer et al. 2004), or for high obscuration, or a combination of both. 4 of the 15 sources have no detection in the soft band suggesting high obscuration, possibly combined with high redshift. More details about the sample selection can be found in Civano et al. (2011) and are also presented in Fig. 2.

2.2 The ChaMP sample

The ChaMP is a wide-area non-continuous X-ray survey based on archival X-ray images of the high Galactic latitude ($|b| > 20$ deg) sky observed with ACIS on *Chandra*. The flux levels (in erg cm^{-2} s^{-1}) reached in the survey are 9.4×10^{-16}–5.9×10^{-11} in the full (0.5–8 keV), 3.7×10^{-16}–2.5×10^{-11} (0.5–2 keV) in the soft and 1.7×10^{-15}–6.7×10^{-11} (2–8 keV) in the hard band, respectively. The ChaMP survey includes a total of 392 fields, omitting pointings from dedicated serendipitous surveys like C-COSMOS, the *Chandra* Deep Fields, as well as fields with extended (>3 arcmin) bright optical or X-ray sources. The list of *Chandra* pointings avoids any overlapping observations by eliminating the observation with the shorter exposure time. The survey has detected a total of >19 000 X-ray sources (Kim et al. 2007; Green et al. 2009) over 33 deg^2 with ∼15 350 X-ray sources positionally matched to SDSS optical counterparts (Green et al. 2009).

The study of the X-ray-detected AGN properties requires accurate estimation of redshifts, luminosities and source classification thus, good quality spectra or, when not available, multiband photometry. Hence for our X-ray analysis we chose only the 323 fields overlapping with SDSS DR5 imaging for which the sensitivity curve is given by Green et al. (2009), to determine accurate number counts. Optical spectroscopy of ChaMP X-ray sources was described by Trichas et al. (2012), where redshifts and classifications for a total of 1569 *Chandra* sources are presented. Since the ChaMP is a *Chandra* archival survey, most ChaMP fields contain targeted sources selected by the target's PI, and those targets are likely to be biased towards special X-ray populations such as bright AGN. Of the targeted sources ∼90 per cent have a secure spectroscopic redshift with 33 of them having at $z > 3$ and 29 at $z > 4$ (see Trichas et al. 2012). The high rate of high-redshift-detected sources clearly shows the strong selection biases that could affect our analysis if we included the targeted sources. Therefore, we exclude all targeted sources (153) to reduce bias in sample properties and source number counts.

For SDSS point sources with $i < 21$ and without available spectroscopy, efficient photometric selection of quasars is possible using a nonparametric Bayesian classification based on kernel density estimation as described in Richards et al. (2009). To select high-z candidates without available spectroscopic or photometric redshift, SDSS detection is required in at least the i and z bands, to detect Lyman dropouts (e.g. Steidel et al. 1996).

Searching the ChaMP catalogue for X-ray sources within 4 arcsec of the optical SDSS quasar coordinate (95 per cent of the matched sample has an X-ray/optical position difference of less than 3 arcsec; see Green et al. 2009), yields 9727 unique matches (∼63 per cent of the total ChaMP X-ray-selected sample). We additionally searched for cross-matches in the *Wide-field Infrared Survey Explorer* (*WISE*; Wright et al. 2010) and UKIRT (UK Infrared Telescope) Infrared Deep Sky Survey (UKIDSS; Warren, Hewett & Foltz 2000; Hewett et al. 2006; Maddox et al. 2008).[1]

For a source to be included in the *WISE* All Sky Source Catalog (Wright et al. 2010), an SNR > 5 detection was required for one of the four photometric bands, *W*1, *W*2, *W*3, or *W*4, with central wavelengths of roughly 3.4, 4.6, 12, and 22 μm, and angular resolutions of 6.1, 6.4, 6.5, and 12.0 arcsec. Because of the different spatial resolutions, 6.0 arcsec (*WISE*; *W*1) and 1–2 arcsec (SDSS), we use 6 arcsec as the matching radius for *WISE* counterparts (Wu et al. 2012).

[1] The UKIDSS project is defined in Lawrence et al. (2007). UKIDSS uses the UKIRT Wide Field Camera (WFCAM; Casali et al. 2007) and a photometric system described in Hewett et al. (2006). The pipeline processing and science archive are described in Hambly et al. (2008).

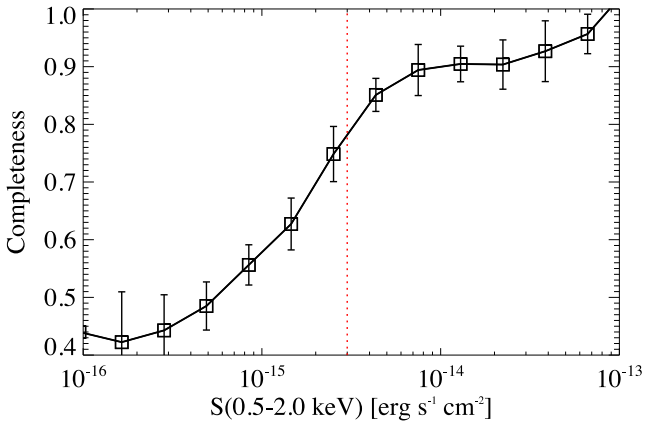

Figure 3. Optical and/or infrared ChaMP survey completeness as a function of 0.5–2 keV X-ray flux. The red dotted line indicates the ChaMP X-ray flux cut with >75 per cent completeness from SDSS/UKIDSS/*WISE*.

Similarly, we searched the UKIDSS Large Area Survey (LAS; Lawrence et al. 2007) Data Release 10 for NIR counterparts to ChaMP X-ray sources. The photometric system is described in Hewett et al. (2006), and the calibration is described in Hodgkin et al. (2009). We used the LAS *YJHK* source table, which contains only fields with coverage in every filter and merges the data from multiple detections of the same object. The X-ray source catalogues were then matched within 3 arcsec of the X-ray position separately to each UKIDSS band: *Y* (0.97–1.07 μm), *J* (1.17–1.33 μm), *H* (1.49–1.78 μm), and *K* (2.03–2.37 μm) recovering also the areas with coverage in a single UKIDSS band. The individual band lists were then combined. For objects not detected in a UKIDSS band, we use the 5σ detection limits provided in Dye et al. (2006) of $Y = 20.23$, $J = 19.52$, $H = 18.73$, and $K = 18.06$. Matching the ChaMP catalogue to *WISE* and UKIDSS, we find 1103 additional *WISE* and/or UKIDSS counterparts which do not have a SDSS counterpart (the detailed numbers are reported in Fig. 2).

In summary, ∼70 per cent of the total ChaMP X-ray sample have SDSS and UKIDSS/*WISE* photometry (9727 SDSS and/or *WISE* and/or UKIDSS and 1103 *WISE* and/or UKIDSS). The limited fraction of optical matches shows how optical counterparts of faint X-ray sources are fainter than the SDSS magnitude limit ($i = 21.0$). SDSS quasars were identified to $i < 19.1$ for spectroscopy by their UV-excess colours, with an extension for $z > 3$ quasars to $i = 20.2$ using *ugri* colour criteria (Richards et al. 2002).

Based on the X-ray limits, the identification completeness of ChaMP X-ray sources falls rapidly for objects with fainter optical counterparts. Fig. 3 shows the optical (SDSS *i*-band counterparts) and infrared (*WISE* and UKIDSS counterparts) completeness of the X-ray-selected sample as a function of the soft (0.5–2 keV) X-ray flux. This incompleteness can severely bias determination of the number counts and space density, particularly at high redshifts (e.g. Barger & Cowie 2005).

To address this issue, we set a relatively high X-ray flux limit in ChaMP, where spectroscopic completeness is higher, and photometric coverage allows good photometric redshifts. We use a soft flux limit for ChaMP at $S_{0.5\text{–}2\,\mathrm{keV}} > 3 \times 10^{-15}$ erg s^{-1} cm^{-2} as at these brighter fluxes the completeness is higher than ≥75 per cent (see Fig. 3). The completeness fraction as a function of flux has

been taken into account for the estimation of the number counts and comoving space density (see Sections 4 and 5). For sources not detected in the soft band, the 0.5–2 keV flux has been computed by converting the 2–10 keV flux using $\Gamma = 1.8$ (see Section 3.2). One of the main advantages of our compilation is that we do not miss the faint high-redshift population, since this is recovered by the C-COSMOS survey. In this way, the ChaMP sample is used for the determination of the bright end of the luminosity function at high redshifts.

2.2.1 *Spectroscopic redshifts*

We compiled secure spectroscopic redshifts for a total of 1547 sources. We have used 1056 sources (excluding target sources) from existing ChaMP spectroscopy (Trichas et al. 2012) for the selected ChaMP fields. Additional spectroscopic redshifts are given in the SDSS-III ($N = 91$; Noterdaeme et al. 2012) and SDSS-DR10 quasar catalogues ($N = 145$; Pâris et al. 2014). We also searched the literature by cross-correlating optical positions with the NASA Extragalactic Database (NED), using a 2 arcsec match radius where we found 255 more sources with spectroscopic redshift.

The high-redshift spectroscopic sample consists of 44 sources with $z > 3$. All of these sources have a soft band X-ray detection, and only three sources lack a hard-band detection. Among them, there are seven sources with $z > 4$ and one source with $z = 6.016 \pm 0.005$ (Jiang et al. 2007). All but six of them have SDSS optical spectra with mean S/N > 4.5 (none of them has S/N < 2.0) with at least two broad emission lines (Lyα and C IV) significantly detected. For five of the remaining sources, redshifts have been obtained by Trichas et al. (2012) while for the source with the highest spectroscopic redshift ($z = 6.016$) we have used the estimate from Jiang et al. (2007). For 30 sources of the ChaMP spectroscopic sample, there are available photometric redshifts derived by Richards et al. (2009, see Section 2.2.2) with an accuracy of $\sigma_{\Delta z/(1+z_{\rm spec})} = 0.013$ and only one catastrophic outlier.

2.2.2 *SDSS photometric redshifts*

For the sources without spectroscopic redshifts, we derived photometric redshifts. The criteria used in SDSS DR6 have now been refined to include objects redder than $(u - g) = 1.0$ which may well be high-z quasars. The resulting catalogue of ∼1 million photometrically identified quasars and their photometric redshifts from SDSS Data Release 6 (DR6) is described in Richards et al. (2009). Only point sources (type = 6) with i-band magnitudes between 14.5 and (de-reddened) 21.3 (psfmag_i > 14.5 and psfmag_i − extinction_i < 21.3; where psfmag are the point-spread-function magnitudes). They estimate the overall efficiency of the catalogue to be better than 72 per cent, with subsamples (e.g. X-ray-detected objects) being as efficient as 97 per cent. At the faint limit of the catalogue some additional galaxy contamination is expected.

There are 1611 sources with SDSS high-quality photometric redshifts and no spectroscopic redshifts in ChaMP (i.e. those with good ≥ 0.0, where good is the quality flag; 6 = most robust; −6 = least robust; Richards et al. 2009). Among them there are 14 sources with $z_{\rm phot} > 3$ and one with $z_{\rm phot} > 4$, above the adopted ChaMP flux limit. All of these sources are detected in both soft and hard band. The SDSS photo-z code also gives a probability of an object being in a given redshift range. In this way, we have not only the most likely redshift but also the probability that the redshift is between some minimum and maximum value, which is crucial for dealing with catastrophic failures. The redshift probability distribution for each source is taken into account for the estimation of the number counts and comoving space density (see Sections 4 and 5). As for C-COSMOS selection of high-z sources, we also included 13 sources having $z_{\rm photo} + 1\sigma_{\rm zphoto} > 3$ and $z_{\rm photo} < 3$. This adds another 10 objects to the main sample, all of them detected in both soft and hard bands.

Table 1. Photometric redshift reliability defined by Wu et al. (2012) and number of sources for ChaMP sources without spectroscopic or SDSS photometric redshifts.

Surveys[a]	Reliability (per cent)	$N_{\rm obj}$[b]	$N_{\rm obj-lim}$[c]
W		955	359
U		27	19
U+W	67.4	19	16
S	70.4	637	367
S+W	77.2	733	526
S+U	84.8	71	44
S+U+W	87.0	238	177
Total		2680	1508

[a]S = SDSS; W = *WISE*; U = UKIDSS.
[b]Number of point-like objects in each combination of surveys.
[c]Number of point-like objects in each combination of surveys with $S_{0.5-2\,\rm keV} > 3 \times 10^{-15}$ erg s^{-1} cm^{-2}.

2.2.3 *High-z candidate selection and photometric redshift estimation*

For the remaining 7759 without a spectroscopic or photometric SDSS redshift, we selected the high-redshift AGN candidates using their optical and/or their infrared colours. Most of these sources (∼70 per cent), despite being included in SDSS DR6 catalogue, were rejected from Richards et al. (2009) selection criteria. The remaining sources come from later SDSS data releases.

Following the same morphological criteria as Richards et al. (2009), a candidate is required to be unresolved in images taken through the two redder filters (e.g. g and r for $z \sim 3$ selection). This minimizes contamination from low-z galaxies since even type-2 AGN at $z > 3$ appear point like. However, we avoid using any faint flux cut in order to ensure that we do not miss faint high-z candidates since non-detection can imply high-z dropouts. We reject sources with flags indicating that their photometry may be problematic (e.g. blending of close pairs of objects, objects too close to the edge of the frame, objects affected by a cosmic ray hit). Overall, we reject 5079 non-point like sources or with problematic photometry. This number (∼65 per cent) is in good agreement with the rejected number of sources by Richards et al. (2009) using the same criteria which explain the lack of a photometric redshift for these sources.

Photometric redshift criteria must strike a quantifiable balance between completeness and efficiency, i.e. a probability can be assigned both to the classification and the redshift. Using the SDSS, UKIDSS, and *WISE*[2] photometric data can help us to select quasar candidates more efficiently than using each survey individually (see Table 1). The photometric redshift reliability, defined by Wu et al.

[2] We use the colours related to *WISE W3* and *W4* magnitudes only for sources lacking SDSS and/or UKIDSS detections because *WISE* uncertainties are substantially larger (Wu, Zhang & Zhou 2004).

(2012) as the fraction of the sources with the difference between the photometric and spectroscopic redshifts smaller than 0.2 is given in Table 1. The highest reliability can be reached only in the UKIDSS surveyed area, which is much smaller (4000 deg^2) than the sky coverage of both SDSS and *WISE* surveys.

Richards et al. (2002) used a 3D multicolour space to select high-redshift QSO candidates in SDSS: *griz* ($g - r$, $r - i$, $i - z$) for candidates with $z > 3.0$. Following the SDSS group, we search for high-z candidates in three redshift intervals ($z \simeq 3.0$–3.5, $z \simeq 3.5$–4.5, $z \simeq 4.5$). The details of the selection criteria are given in the appendix. Our selection criteria require that our sources lie outside of a 2σ region surrounding the stellar locus. We still expect the sample to be contaminated by stars and low-z galaxies. For this reason, we use some additional criteria described by Richards et al. (2002) to exclude objects in colour regions containing predominantly white dwarfs, A stars and unresolved red–blue star pairs. During the colour selection process, no specific line is drawn between optically selected quasars (type-1 AGN) and type-2 AGN. Taking into account that both type-1 and type-2 AGNs are unresolved in optical images at $z > 3$ and type-2 AGNs should lie outside the stellar locus due to their red optical colours, we expect that the above criteria efficiently select both high-redshift AGN populations. We found 53 SDSS-detected high-z candidates.

To increase the reliability of the photometric estimation, we also combine the SDSS selection with the redder baselines from UKIDSS and *WISE*, where the contamination of the stellar locus and low-redshift galaxies is lower. We used the combination of UKIDSS and SDSS colours in the $Y - K$ versus $g - z$ colour–color diagram suggested by Wu & Jia (2010) to efficiently separate quasars with redshift $z < 4$ from stars. Similarly, Wu et al. (2012) suggested that $z - W1$ and $g - z$ colours could be used to separate stars from quasars. Based on these criteria, we have rejected 10 sources associated with stars based on both SDSS–UKIDSS and SDSS–*WISE* colour–color diagrams. For sources detected only by UKIDSS, we used the $i = 21.3$ upper limit and a $Y - K$ versus $i - Y$ colour–color diagram to separate stars and low-z galaxies from high-z candidates. We found four high-z candidates. In the case of sources detected only by *WISE*, there is no efficient way detailed in the literature to separate high-z quasars from stars.

Photometric redshifts have been estimated for the high-z candidates by comparing the observed colours with theoretical colour–redshift relations derived from samples with known redshifts (Richards et al. 2002; Wu & Jia 2010; Wu et al. 2012). A standard χ^2 minimization method is used to estimate the most probable photometric redshifts. Here, the χ^2 is defined as (see Wu et al. 2004)

$$\chi^2 = \sum_{ij} \frac{[(m_{i,cz} - m_{j,cz}) - (m_{i,\mathrm{ob}} - m_{j,\mathrm{ob}})]^2}{\sigma^2_{m_{i,\mathrm{ob}}} + \sigma^2_{m_{j,\mathrm{ob}}}}, \quad (1)$$

where the sum is obtained for all four SDSS colours and/or *WISE* and/or UKIDSS colours, $m_{i,cz} - m_{j,cz}$ is the colour in the colour–redshift relations, $m_{i,\mathrm{ob}} - m_{j,\mathrm{ob}}$ is the observed colour of a quasar, and $\sigma_{m_{i,\mathrm{ob}}}$ and $\sigma_{m_{j,\mathrm{ob}}}$ are the uncertainties of observed magnitudes in two bands. The uncertainty in the measurement was obtained by mapping the $\Delta\chi^2$ error. Since the above studies are dominated by optically selected quasars, we would expect that the photometric redshifts uncertainties in type-1 AGNs are smaller. However, since the Lyα break enters the g band at $z \sim 3.5$, the $g - r$ colours quickly redden with redshift for both populations. Alexandroff et al. (2013) found that $g - r$ colours are indistinguishable at an 84 per cent confidence level between type-1 and type-2 quasars at $z > 2$ suggesting that even in the case of type-2 AGNs the photometric redshifts are reliably estimated. Overall, we found eight sources with $z > 3$ at greater than 1σ significance, four sources with $z > 3$ but lower than 1σ significance, and two sources with $z_{\mathrm{phot}} + 1\sigma_{\mathrm{phot}} > 3$.

2.2.4 *The ChaMP high-z sample*

The total $z > 3$ ChaMP sample includes 87 sources with $z > 3$. Among them there are 44 sources with secure spectroscopic redshift, 15 sources with SDSS $z_{\mathrm{phot}} > 3$ and 13 sources with SDSS $z_{\mathrm{phot}} + 1\sigma_{\mathrm{phot}} > 3$ available from Richards et al. (2009), and 15 sources with estimated photometric redshifts based on optical/infrared colour–redshift relations (13 with $z_{\mathrm{phot}} > 3$ and 2 with $z_{\mathrm{phot}} + 1\sigma_{\mathrm{phot}} > 3$).

3 THE C-COSMOS AND CHAMP $z > 3$ AGN SAMPLE

In summary, we have assembled a sample of X-ray-selected AGNs at $z > 3$ in the C-COSMOS and ChaMP on the basis of both spectroscopic and photometric redshifts. The total sample includes 209 sources with $z > 3$. Of these, 45 are selected to be at $z > 3$ from their broad $P(z)$. There are also 15 C-COSMOS sources considered to be at $z > 3$ on the basis of their optical non-detection these are included only in the derivation of the upper boundary of the $\log N$–$\log S$ curve. The properties of the sample members are given in Table A1 (Appendix A) and the detailed numbers are given in Fig. 2. Fig. 4 shows the optical and near-infrared (i, K, and 3.6 μm) observed magnitude distributions for the total high-z population and for sources with spectroscopic and photometric redshifts, separately. Sources selected as i-dropouts are also presented.

The hard (2–10 keV rest-frame) X-ray luminosity versus plane is shown in Fig. 5 together with the flux limit of the C-COSMOS and ChaMP surveys (dashed line) and the applied flux cut for ChaMP (dotted line). Luminosities were computed from in every case assuming an intrinsic $\Gamma = 1.8$.

The C-COSMOS and ChaMP high-z sample is a factor of 4–5 larger than all the previous individual X-ray-selected samples at $z > 3$ (e.g. Brusa et al. 2009; Hiroi et al. 2012; Vito et al. 2013). Most importantly, this is the first time that a significant sample of 29 X-ray-selected AGNs at $z > 4$ is assembled. At these redshifts previous studies had a maximum of nine sources. The $z > 3$ X-ray-selected AGN sample also covers more than a factor of 2 of soft (2–10 keV rest-frame) X-ray luminosity, and includes a significant number of both broad-line and non-broad-line AGNs.

To discuss the obscured AGN fraction requires each object in our sample to be classified as obscured or unobscured. There are two commonly adopted methods for classification: one is based on the optical emission line widths ('optical type') or, if a spectrum is not available, by the type of template that best fits the optical–infrared SEDs of the sources. The other is based on the column densities, N_{H}, in the X-ray spectra ('X-ray type') or, if an X-ray spectrum is unavailable, by the hardness ratio (HR; e.g. Hasinger et al. 2001). X-ray absorption should typically correlate with optical AGN type. In the unified scheme (e.g. Lawrence & Elvis 1982; Antonucci 1993; Urry & Padovani 1995) as the narrow emission line AGNs are viewed through the dusty torus, and hence have higher absorption column densities than broad emission line AGNs. In fact, evidence has been mounting over the years that the optical- and X-ray-based classifications often give contrasting results (Lawrence & Elvis 2010; Lanzuisi et al. 2013; Merloni et al. 2014).

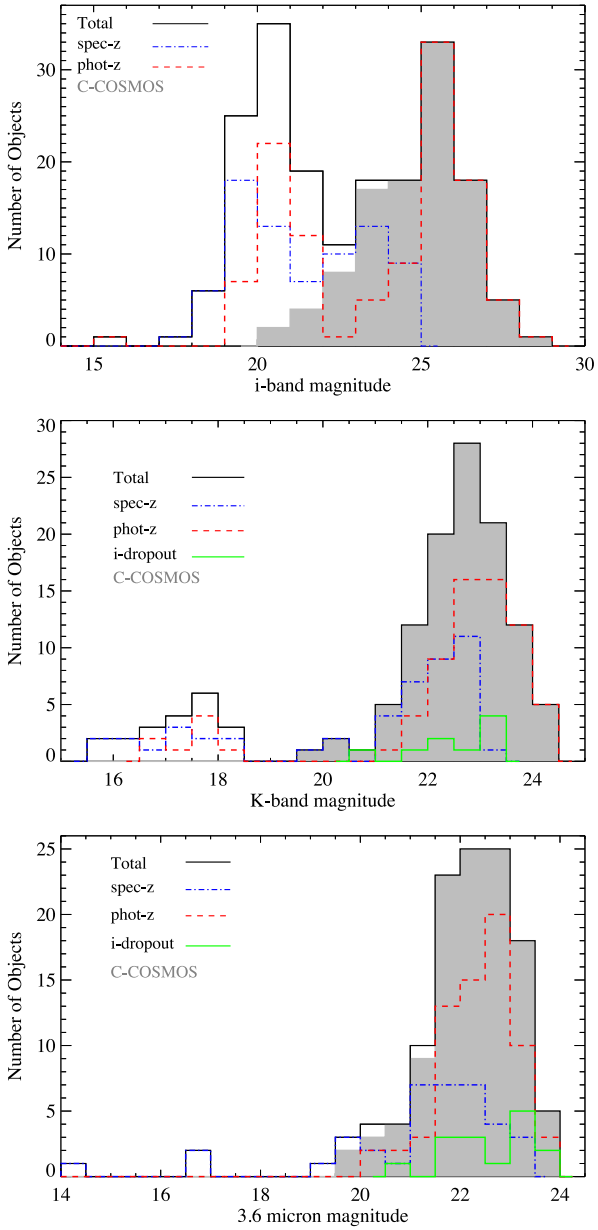

Figure 4. Observed AB magnitude distribution of all the *i*-band, *K*-band, and 3.6 μm band (from top to bottom) high-z objects. Black solid, blue dot–dashed, red dashed, and green solid lines represent the total, spectroscopic, photometric redshift, and *i*-dropout samples, respectively. The *i*-band dropouts are not included in the *i*-band histogram.

3.1 Optical types

The optical type of the sources has been determined by the measured full width at half-maximum (FWHM) of the permitted emission lines. Those objects with emission lines having FWHM >1000 km s^{-1} (e.g. Stern & Laor 2012) are classified as 'optical broad-line' (BLAGN), and all others as 'optical non-broad-line' (non-BLAGN), i.e. they show narrow emission lines or absorption lines only, following Civano et al. (2011, 2012).

In the C-COSMOS spectroscopic $z > 3$ sample, 21 of 32 sources are classified as BLAGN. These are mainly associated with the brighter optical sources ($i_{AB} \sim 22$–23) of the spectroscopic sample (see Fig. 7). At fainter optical magnitudes ($i_{AB} > 23$), equal

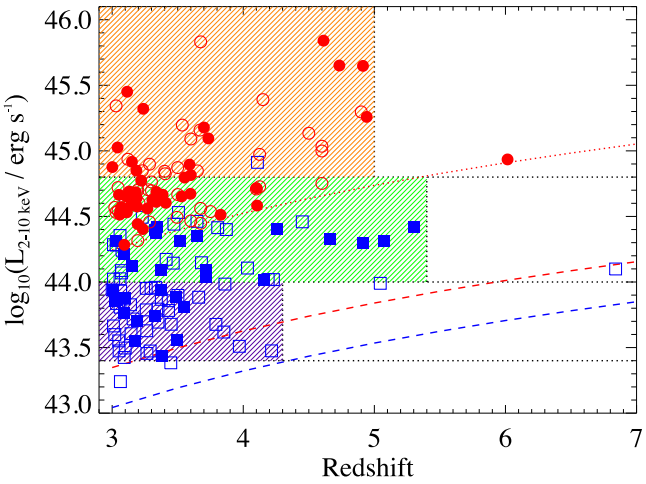

Figure 5. The hard X-ray luminosity (computed with $\Gamma = 1.8$) redshift plane for the objects in our sample. Blue squares = C-COSMOS sample. Red circles = ChaMP sample. Filled = spectroscopic redshift. Open = photometric redshift. The dashed lines represent the 2–10 keV luminosity limit of the surveys computed from the 0.5–2 keV limiting flux. The dotted red line represents the completeness flux cut we have adopted at 3×10^{-15} erg cm^{-2} s^{-1}. The dotted black lines correspond to the flux limits we imposed for the computation of the space density and their associated areas, purple ($43.4 < \log L_X < 44.0$), green ($44.0 < \log L_X < 44.7$), orange ($\log L_X > 44.7$).

numbers of broad-line and non-broad-line AGNs are found. The classification for the 75 AGNs in C-COSMOS with photometric redshifts is obtained by the Salvato et al. (2011) photometric fitting method fitting the SED via χ^2 minimization with code LEPHARE (Arnouts & Ilbert 2011).[3] More details on the fitting can be found in Salvato et al. (2011). Briefly, two libraries of templates were used, depending on morphology, optical variability, and X-ray flux of the source. The first library (defined in Salvato et al. 2009, table 2) consists of AGN templates, hybrid (host + AGN) templates, and a few normal galaxies and was used for all the point-like optical sources and for the extended sources with an X-ray flux brighter than 8×10^{-15} erg cm^{-2} s^{-1}. The second library (as defined in Ilbert et al. 2009) includes only normal galaxy templates and it was used for the remaining sources (i.e. extended and with X-ray flux $<8 \times 10^{-15}$ erg cm^{-2} s^{-1}). The flowchart in fig. 6 of Salvato et al. (2011) summarizes the procedure. Civano et al. (2012), according to this fitting, divide the sources into obscured AGN, galaxies and unobscured AGN. About 40 per cent (28 sources) of the photometric sample is best fitted with an unobscured quasar template, and 47 sources with an obscured quasar template. For 29 AGNs with spectroscopic identification, the photometric and spectroscopic types match. Given the mismatch rate of ∼9 per cent, we estimate that ∼7 out of the 75 AGNs could have been assigned the wrong SED classification.

In the ChaMP $z > 3$ spectroscopic sample, as expected at these fluxes (e.g. Brusa et al. 2009), and due to the predominantly SDSS spectroscopic target selection, only 2/44 sources are non-BLAGN. The characterization of these sources based on their SED fittings has been obtained by Trichas et al. (2012). In order to be in agreement with the spectroscopic ChaMP sample, we followed the same SED fitting method for the characterization of the 43 sources without a spectroscopic classification. According to this fitting, 11 of

[3] http://www.cfht.hawaii.edu/arnouts/LEPHARE/lephare.html

43 sources are best fitted with an obscured quasar template (non-BLAGN). More details on the fitting can be found in Trichas et al. (2012) and Ruiz et al. (2010). Briefly, a total of 16 templates has been used including QSO, Seyfert-2 galaxies, starburst galaxies, absorption line galaxies and composite templates that are known to harbour both an AGN and a starburst. The Ruiz et al. (2010) model has been adopted, which fits all SEDs using a χ^2 minimization technique within the fitting tool SHERPA (Freeman, Doe & Siemiginowska 2001). The fitting allows for two additive components, one associated with the AGN emission and the other associated with the starburst emission. The fit with the lowest reduced χ^2 has been chosen as the best-fitting model.

A general problem of relying on the optical type is that the classification may depend on the quality of the available optical spectra, since good signal-to-noise ratio is required to detect less-luminous broad-emission lines above the stellar continuum emission of host galaxies. Also, at $z > 3$, the Hα emission line moves into the infrared and so, until recently, was difficult to observe. Intermediate AGN types (1.8, 1.9; Osterbrock & Koski 1976) rapidly lose their broad Hβ emission, and without Hα these may be misclassified as type-2. Nevertheless, such effects are not expected to be significant in our sample, as t consists predominantly of luminous AGNs for which contamination from the host galaxies is negligible.

3.2 X-ray types

Most sources in our sample have a low number of detected counts (median ∼25 in the 0.5–8.0 keV full band). In this count regime, spectral fit results are not reliable, especially if more than one free parameter is fitted; even if the fit converges the uncertainties on the parameters are large. For these reasons, we use the Bayesian Estimation of Hardness Ratios (BEHR) method (Park et al. 2006) to derive X-ray spectral type. Hardness count ratios (HR), defined as HR $= (C_{\rm HB} - C_{\rm SB})/(C_{\rm HB} + C_{\rm SB})$, where $C_{\rm SB}$ and $C_{\rm HB}$ are the counts in the soft band and hard band, respectively.

BEHR is particularly powerful in the low-count Poisson regime, because it computes a realistic uncertainty for the HR, regardless of whether the X-ray source is detected in both energy bands. Sources with unconstrained upper or lower limits due to non-detections (14 hard-only and 49 soft-only detections) have been computed by converting the 3σ flux upper limit in the undetected band into counts.

To estimate the column density, curves of constant $N_{\rm H}$ as a function of redshift have been derived for two spectral slope values, $\Gamma = 1.4$ and $\Gamma = 1.8$. The flatter spectral slope has been chosen to be consistent with the assumptions adopted in producing the original X-ray catalogues (Kim et al. 2007; Puccetti et al. 2009). The steeper value is more representative of the intrinsic value if the spectrum is not affected by obscuration (Nandra & Pounds 1994). The relationship between HR and redshift of our C-COSMOS and ChaMP AGN samples is shown in Fig. 6. Curves of $N_{\rm H} = 10^{20}$, 10^{22}, 5×10^{22}, and 10^{23} cm^{-2} are reported for $\Gamma = 1.8$ (dashed lines) and $\Gamma = 1.4$ (solid lines). We observe that C-COSMOS sample tend to be more obscured as expected due to the fainter X-ray sensitivity limit, than the ChaMP sample (Lawrence & Elvis 1982; Ueda et al. 2003; Hasinger 2008; Brusa et al. 2010; Burlon et al. 2011).

Though the two samples (C-COSMOS and ChaMP) of $z > 3$ AGNs show different trends regarding their obscuration, the large HR errors and the similarity in this redshift range of the curves with widely different $N_{\rm H}$ values for the same spectral slope, do not allow an accurate estimate of the column density for each source

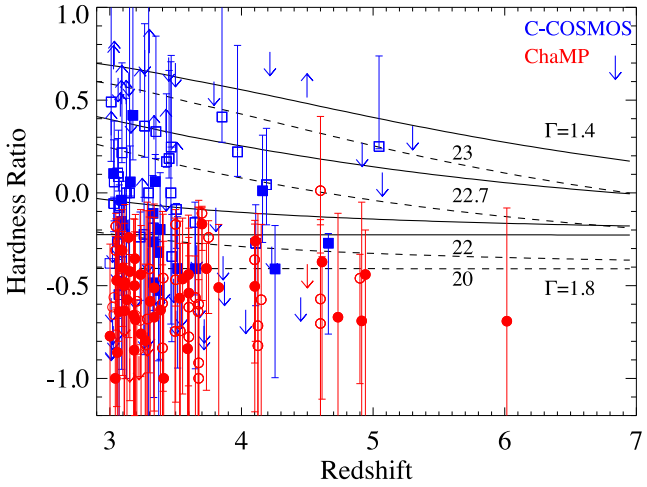

Figure 6. HR versus redshift. Blue squares = C-COSMOS sample. Red circles = ChaMP sample. Filled = spectroscopic redshift. Open = photometric redshift. Sources with no hard band or soft band detection are shown with arrows. Four curves of constant $N_{\rm H}$ (10^{20}, 10^{22}, 5×10^{22}, and 10^{23} cm^{-2}) are reported for $\Gamma = 1.8$ (dashed lines) and $\Gamma = 1.4$ (solid lines).

to be made. Using the CIAO[4] spectral analysis package, SHERPA,[5] we have simulated X-ray spectra for AGN populations at $3 < z < 7$ in order to quantify the evolution of X-ray spectral slopes due to the k-correction of the observed AGN spectra towards high-z. Based on these simulations, we find that the HR distribution for the ChaMP sample peaks at $\Gamma \sim 1.8$–2.0 while the HR distribution for C-COSMOS sample peaks at $\Gamma \sim 1.4$–1.9. Hereafter, to better constrain the column density and for the purpose of comparison with previous studies, we fixed the photon index to $\Gamma = 1.8$ and converted all source fluxes.

In this work, we adopt $N_{\rm H} = 10^{22}$ cm^{-2} as the dividing criterion; AGNs with $N_{\rm H} < 10^{22}$ cm^{-2} and $>10^{22}$ cm^{-2} are classified as X-ray unobscured and obscured, respectively. This criterion is adopted by many authors, and is known to be generally in good agreement with the optical type (see e.g. Ueda et al. 2003; Hiroi et al. 2012).

3.3 X-ray/optical flux ratio

The X-ray/optical (X/O) flux ratio is a redshift dependent quantity for obscured AGN, given that the k-correction is negative in the optical band and positive for the X-rays (Comastri et al. 2003; Fiore et al. 2003; Brusa et al. 2010). As a result, obscured sources have higher X/O at high redshift. On the other hand, unobscured sources have similar k-corrections in the two bands, and the distribution in X/O is not correlated with the redshift (Civano et al. 2012). Usually, the r- or i-band flux is used (e.g. Brandt & Hasinger 2005) while a soft X-ray flux was used originally used for this relation with the majority of luminous spectroscopically identified AGNs in the Einstein and ASCA surveys characterized by X/O $= 0 \pm 1$ (e.g. Stocke et al. 1991; Schmidt et al. 1998; Lehmann et al. 2001). The same relation has been used also in the hard band, without really accounting for the X-ray band used or the change in spectral slope (e.g. Alexander et al. 2001; Brusa et al. 2003; Fiore et al. 2003; Civano, Comastri & Brusa 2005; Laird et al. 2009; Xue et al. 2011).

Fig. 7 shows the distribution of X-ray soft (left) and hard (right) flux versus optical magnitude to illustrate the parameter space

[4] http://cxc.harvard.edu/ciao/
[5] http://cxc.harvard.edu/sherpa/

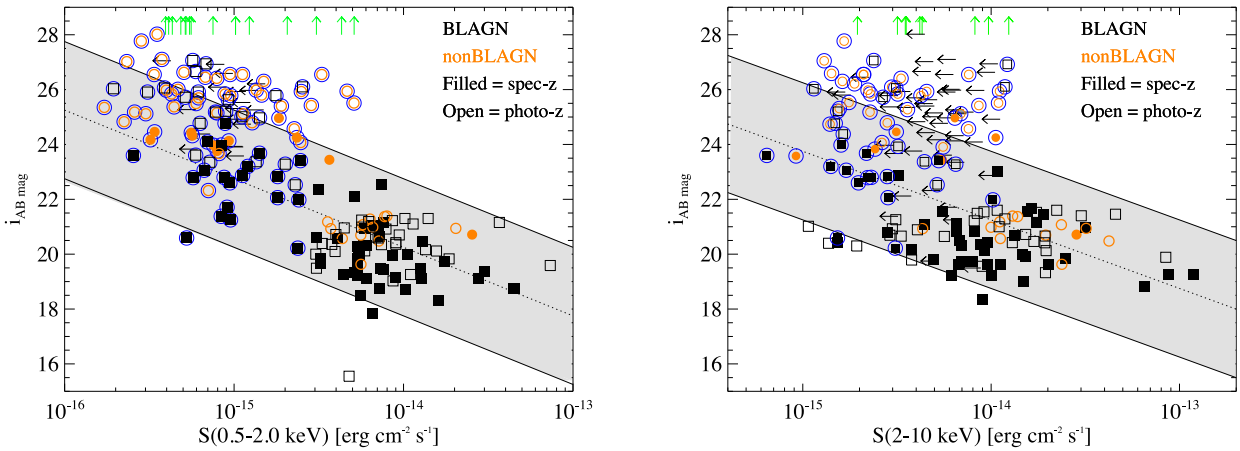

Figure 7. X-ray flux (soft-left, hard-right) versus the *i*-band magnitude for all the X-ray sources with an *i*-band counterpart. The grey shaded region represents the locus of AGNs along the correlation X/O = 0 ± 1. Sources with secure spectroscopic redshifts are represented by filled symbols and sources with a photometric redshift by open symbols. Orange circles and black squares represent non-BLAGN and BLAGN, respectively. Green upper limits represent *i*-band dropouts and black left pointing arrows represent soft and hard X-ray flux upper limits for undetected sources in each band. The C-COSMOS sample is represented by the open big blue circles.

spanned by the broad-line and non-broad-line populations. The X/O ratio (Maccacaro et al. 1988) is defined as

$$\mathrm{X/O} = \log_{10}(f_\mathrm{X}/f_\mathrm{opt}) = \log_{10}(f_\mathrm{X}) + C + m_\mathrm{opt}/2.5, \quad (2)$$

where f_X is the X-ray flux in a given energy range, m_opt is the magnitude at the chosen optical wavelength, and C is a constant which depends on the specific filter used in the optical observations. For both X-ray bands, the X/O = ±1 locus (grey area) has been defined using as $C(i) = 5.91$ (Civano et al. 2012), which was computed taking into account the width of the *i*-band filters in Subaru, CFHT (Canada–France–Hawaii Telescope), or for bright sources SDSS. In the hard band, the locus is plotted taking into account the band width and the spectral slope used to compute the X-ray fluxes ($\Gamma = 1.8$). The majority of BLAGNs with a secure spectroscopic redshift, follow the trend of $-1 < \log_{10}(f_\mathrm{X}/f_i) < 1$. However, given the variation in α_OX with luminosity (e.g. Vignali, Brandt & Schneider 2003; Young, Elvis & Risaliti 2010; Trichas et al. 2013), there can be some shift in the locations of QSOs with luminosity within the so-called BLAGN region. This shift is consistent with the X/O relation being originally calibrated on soft-X-ray-selected sources, bright in the optical and also in the X-rays. This might explain the mild shift between the ChaMP and C-COSMOS BLAGNs.

Apart from the AGN population found in the BLAGN region, there is also a significant population that lie at $\log_{10}(f_\mathrm{X}/f_i) > 1$ suggesting obscured nuclei. The main characteristics of this sample are as follows: (1) lack of spectroscopic redshifts (open symbols), (2) non-BLAGN optical classification (green symbols), and (3) low X-ray luminosities ($10^{43}\,\mathrm{erg\,s^{-1}} < L_{2-10\,\mathrm{keV}} < 10^{44}\,\mathrm{erg\,s^{-1}}$) with $N_\mathrm{H} > 10^{22}\,\mathrm{cm^{-2}}$ for ∼65 per cent of them, which is consistent with previous studies finding that mild obscuration is common at these luminosities (e.g. Silverman et al. 2010). Furthermore, nearly 75 per cent of all the sources with X/O > 1 are obscured, thus confirming that selections based on high X/O ratio are efficient in finding samples of obscured AGNs.

3.4 Comparison of optical and X-ray types

X-ray absorption is an alternative good indicator of AGN type. In order to compare our optical classification to the expected obscuration of BLAGNs and non-broad-line AGNs based on the unified scheme, we have separated our total sample into broad-line and non-broad-line AGNs (as described in Section 3.1).

In the case of the BLAGNs, the X-ray classification criterion ($N_\mathrm{H} = 10^{22}\,\mathrm{cm^{-2}}$) gives 28/124 X-ray obscured sources for $\Gamma = 1.8$. Half of these sources have a spectroscopic redshift and all but three come from C-COSMOS sample. If we also take into account the HR errors, then for the lower HR limits, 11 BLAGNs are classified as X-ray obscured sources and 41 are classified X-ray obscured sources for the upper HR limits. In the non-BLAGN subset, the above criterion gives 49/71 X-ray obscured sources (detected in both soft and hard bands) for $\Gamma = 1.8$. The 27 soft band sources in non-BLAGN sample with no detection in the hard band (reported as downward arrows in Fig. 6) have very high upper limits on the HR, due to the conservative flux upper limit computed by Puccetti et al. (2009), but most of them do not thereby satisfy the $N_\mathrm{H} > 10^{22}\,\mathrm{cm^{-2}}$ criterion.

For the total sample, we find agreement between the optical and X-ray classification for ∼74 per cent: ∼77 per cent for the BLAGNs and ∼69 per cent for the non-BLAGNs. These rates are consistent with recent studies (e.g. Lanzuisi et al. 2013; Merloni et al. 2014). Possible explanation can be a misclassification of faint type-1 with strong optical/IR contamination from host galaxy light.

To improve the statistics and gain information on the average properties of the two subclasses, we compared their mean HR values as a function of redshift (Fig. 8). Despite the ∼30 per cent misclassification for the individual sources (see Table 2), the mean properties of the BLAGNs and non-BLAGNs seem to agree with the $N_\mathrm{H} \sim 10^{22}\,\mathrm{cm^{-2}}$ division. These results does not change even if we use only sources with spectroscopic redshifts. The upper and lower limits detected only in the soft or the hard band were used to compute the upper and lower boundary of the shaded area. We discuss the results in Section 5.

4 THE log*N* − log*S* OF THE $z > 3$ AGN

We derived the soft band number counts of the $z > 3$ and $z > 4$ samples by folding the observed flux distribution through the sky coverage area versus flux curve of the C-COSMOS survey (Puccetti et al. 2009) and the ChaMP's 323 fields (Green et al. 2009). Additionally, we have corrected the number counts for ChaMP

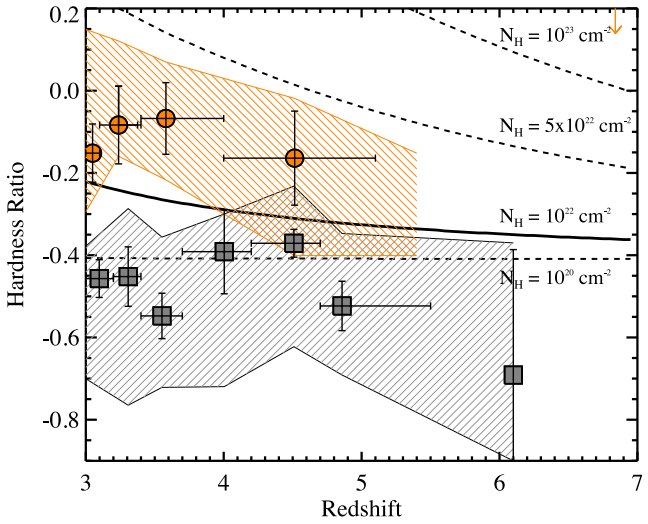

Figure 8. The mean HR as a function of redshift for BLAGN (black squares) and non-BLAGN (orange circles) $z > 3$ AGN subsamples. The error bars represent the 68 per cent dispersion. Only sources with both soft and hard band detections are taken into account for the estimation of the mean HR in each bin. Undetected sources in one of these bands are included only for estimation of the upper and lower limits (dashed areas). The $z_{phot} = 6.88$ source with an upper limit $HR_{up} = 0.74$ has been shifted down to HR = 0.2 in order to be included in the figure.

Table 2. Comparison of optical and X-ray types. The upper and lower limits have been estimated taking into account only the error ranges in HR.

Number of sources	Unobscured $N_H < 10^{22}$ cm^{-2}	Obscured $N_H \geq 10^{22}$ cm^{-2}
BLAGN	96^{+16}_{-14}	28^{+14}_{-16}
Non-BLAGN	22^{+13}_{-9}	49^{+9}_{-13}

incompleteness in the spectroscopic/photometric coverage as a function of X-ray flux (i.e. Fig. 3).

To minimize the error associated with the most uncertain part of the sensitivity curve, we truncate the C-COSMOS sample at the flux corresponding to 10 per cent of the total area (blue dashed line in Fig. 1). All the sources with a 0.5–2 keV flux above 3×10^{-16} erg cm^{-2} s^{-1} have been considered (73 objects out of the 81 soft band detected). The flux limit applied to the sample is consistent with the signal-to-noise ratio thresholds chosen by Puccetti et al. (2009), on the basis of extensive simulations, to avoid the Eddington bias in the computation of the number counts of the entire C-COSMOS sample. Thus, by applying a flux limit cut, we also reduce the Eddington bias affecting our sample. For ChaMP this would be at $S_{0.5-2\,keV} > 2 \times 10^{-15}$ erg cm^{-2} s^{-1}, below the flux limit already applied.

The binned log N–log S relations for two redshift ranges ($z > 3$; orange points and $z > 4$; blue points, with associated errors) are plotted in Fig. 9 (top panel). In integral form, the cumulative source distribution is represented by

$$N(>S) = \sum_{i=1}^{N_S} \frac{1}{\Omega_i}, \quad (3)$$

where $N(>S)$ is the number of sources with a flux greater than S and Ω_i, is the limiting sky coverage associated with the ith source.

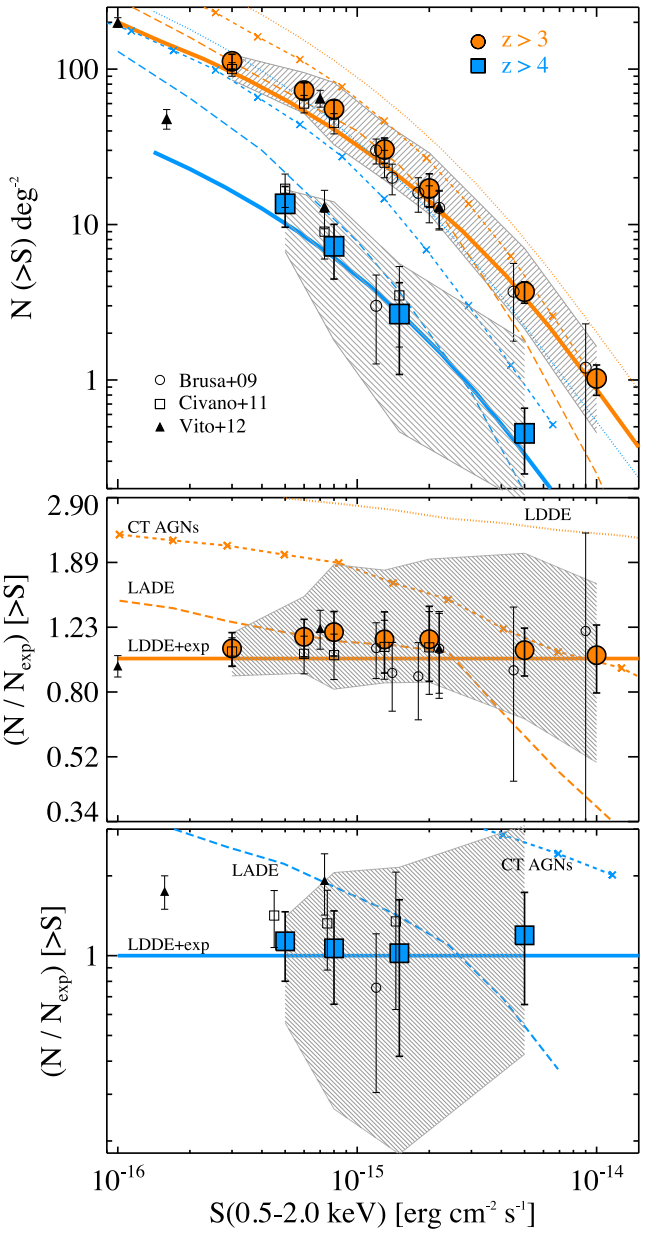

Figure 9. Top: the binned log N–log S relation (with associated errors) of the $z > 3$ (orange circles) and $z > 4$ (blue squares) QSOs population. The grey shaded area represents the maximum and minimum number counts under the assumptions described in Section 4. The blue and orange curves correspond to the prediction based on the LDDE+exp (thick solid), LDDE (dotted), LADE (dashed), and CT AGNs (dash cross) models for each redshift range, respectively. The small open circles represents the number counts estimated by Brusa et al. (2009), the small open squares are from Civano et al. (2011), and small filled triangles from Vito et al. (2013). Middle: the ratio of the observed number counts for $z > 3$ relative to the LDDE+exp model (thick solid line at the top panel). The thick solid line represents the LDDE+exp model $N/N_{exp} = 1$, the dotted line represents the LDDE relative to the LDDE+exp model, the dashed lines the LADE relative to the LDDE+exp model, and the dash cross lines the CT AGNs model relative to the LDDE+exp model. Bottom: the ratio of the observed number counts for $z > 4$ relative to the LDDE+exp model. Symbols are similar to the medium panel. The ratio of the LDDE relative to the LDDE+exp model is $N/N_{exp} > 8.0$ and is not presented.

The associated error is the variance:

$$\sigma^2 = \sum_{i=1}^{N_S} \left(\frac{1}{\Omega_i}\right)^2 \quad (4)$$

The grey shaded area represents an estimate of the maximum and minimum number counts relation at $z > 3$ obtained by considering three different effects:

(1) the 1σ uncertainty in the sky coverage area for each source using the sky coverage as a function of flux (see Fig. 1) and the 1σ uncertainty in the flux;

(2) the 14 sources from C-COSMOS with no-optical detection (seen in the soft band);

(3) the sources with photometric redshift $z_{\rm photo} < 3$ but $z_{\rm photo} + \sigma_{z\rm photo} > 3$.

To compute the upper boundary of the shaded area, we included all the sources in the main sample plus the sources with no optical detection at their flux+1σ error. For the lower boundary, we used the flux-1σ error only for the sources with $z_{\rm spec} > 3$. Under these assumptions, the lower limit corresponds to the (very unlikely) hypothesis that all the photometric redshifts are overestimated, while the upper limit corresponds to the assumption that non-detection in the optical band is a 100 per cent reliable proxy of high redshift in X-ray-selected samples.

We have compared our number counts with previous X-ray surveys that span the range from deep, small area (CDF-S, at 464.5 arcmin^2 with a soft band flux limit of $\sim$9.1 $\times$ 10^{-18} erg cm^{-2} s^{-1}; Xue et al. 2011), to moderate area and moderate depth (*Chandra*-COSMOS at 0.9 deg^2 with a 0.5–2 keV flux limit of $\sim 1.9^{-16}$ erg cm^{-2} s^{-1}; Elvis et al. 2009), and finally to moderate area and shallower depth (*XMM*-COSMOS, at 2 deg^2 and a soft band flux limit of $\sim$1.7 $\times$ 10^{-15} erg cm^{-2} s^{-1}; Cappelluti et al. 2009). The binned $\log N$–$\log S$ relations are plotted in Fig. 9 (top panel), together with the *XMM*-COSMOS (Brusa et al. 2009, open circles), C-COSMOS (Civano et al. 2011, open squares), and 4 Ms CDF-S number counts (Vito et al. 2013, filled triangles).

Good agreement exists among the comparison surveys presented here. At $z > 3$ and fainter X-ray fluxes ($S_{0.5-2\,\rm keV} < 2 \times 10^{-15}$ erg cm^{-2} s^{-1}) our points confirm the agreement with the model predictions, previously found by Brusa et al. (2009), Civano et al. (2011), and Vito et al. (2013). At the same redshift range but brighter X-ray fluxes, where only *XMM*-COSMOS sample have available points (Brusa et al. 2009) based on four sources, we reduce the uncertainties by factor of 4 using a sample of 66 sources with ($S_{0.5-2\,\rm keV} > 2 \times 10^{-15}$ erg cm^{-2} s^{-1}). Notably, it is the first time that data points at the bright end at $z > 4$ are included. At redshift $z > 4$, where the *XMM*-COSMOS sample had only 4 sources, the 4 Ms CDF-S 9 sources and the C-COSMOS 14 sources, the C-COSMOS and ChaMP sample has 27 sources (two to five times larger), making it possible to compare the slope of the counts with models.

A comparison with the AGN number counts from three different phenomenological model predictions is also presented in Fig. 9 with the different types of curves (orange colour for $z > 3$ and blue colour for $z > 4$).

(1) The thick solid lines correspond to the predictions of the XRB synthesis model of Gilli et al. (2007), based on the X-ray luminosity function observed at low redshift (e.g. Hasinger et al. 2005), parametrized with an LDDE and a high-redshift exponential decline with the same functional form adopted by Schmidt, Schneider & Gunn (1995, $\Phi(z) = \Phi(z_0) \times 10^{-0.43(z-z_0)}$ and $z_0 = 2.7$) to fit the optical luminosity function between $z \sim 2.5$ and 6 (Fan et al. 2001), corresponding to one e-folding per unit redshift (hereafter referred to as LDDE+exp).

(2) The dotted curves correspond to the predictions of the LDDE model without the high-z decline (Gilli et al. 2007), obtained extrapolating to high-z the best-fitting parameters of Hasinger et al. (2005).

(3) The dashed line is the LADE model (Aird et al. 2010) which fits the hard X-ray luminosity function derived by Aird et al. (2010) using the 2Ms *Chandra* Deep Fields and the AEGIS-X (200 ks) survey to probe the faint end ($\log L_{\rm X} < 43$ erg s^{-1}) and the high-z ($z \sim 3$) range.

(4) The dash-crossed lines correspond to the Treister, Urry & Virani (2009) X-ray background population synthesis predictions (CT AGNs).[6]

While at $z > 3$ the two model predictions are very close, at $z > 4$, where the models have different slopes, the errors on the data of the previous studies do not allow a firm preference of one of the two models, highlighting the advantage of our sample with respect to previous surveys. In this work, we find that the LDDE model (Gilli et al. 2007) without decline clearly overestimates the observed counts even in the most optimistic scenario (upper boundary) in both the $z > 3$ and $z > 4$ redshift ranges. Our results for the $z > 3$ sample (orange colour) are in good agreement with both LDDE+exp (thick solid line) and LADE (dashed line) model predictions but only up to flux $\sim 2 \times 10^{-15}$ erg cm^{-2} s^{-1}, where the difference of the two models is <20 per cent. However, the main advantage of our sample becomes clear at brighter fluxes; our results strongly exclude the LADE model. This is in contrast to previous studies which could not distinguish between the two models due to their large uncertainties.

At $z > 4$ (blue colour), our results are in good agreement with LDDE+exp predictions. We cannot clearly exclude the LADE model if we take into account the upper and lower boundaries. However, we can point out for first time that there is no sign of the expected decline to higher fluxes. LDDE is fully ruled out at $z > 4$. While fainter samples would be also useful for a better description of the model, considering only the $z > 4$ subsample by Vito et al. (2013, 4 Ms CDF-S, filled triangles), the data lie between the LDDE+exp and LADE models prediction. Vito et al. (2013) have included the presence of 3 sources at $5 < z < 7.7$, whose redshifts are determined on the basis of relatively uncertain photometric information. If these sources were placed at $3 < z < 4$, good agreement would be obtained with the LDDE+exp model (see Vito et al. 2013), fig. 9). In this case, the Vito et al. (2013) $z > 4$ sample would be consisted only by two sources.

5 2–10 keV COMOVING SPACE DENSITY

To investigate the cosmological evolution of AGN at $z > 3$, we calculate the comoving space density from our sample utilizing the $1/V_{\rm max}$ method (Schmidt 1968). This method takes into account the fact that more luminous objects are detectable over a larger volume and is readily adapted to the case in which the survey area depends on flux.

[6] Model predictions from the work of Treister et al. (2009) for a range of input values are publicly available at http://agn.astroudec.cl/j_agn/main.html

The maximum available volume, over which each source can be detected, was computed by using the formula:

$$V_{\rm max} = \int_{z_{\rm min}}^{z_{\rm max}} \Omega(f(L_{\rm X}, z, N_{\rm H})) \frac{{\rm d}V}{{\rm d}z} {\rm d}z,$$

where $\Omega(f(L_{\rm X}, z, N_{\rm H}))$ is the sky coverage at the flux $f(L_{\rm X}, z)$ corresponding to a source with absorption column density $N_{\rm H}$ and observed luminosity $L_{\rm X}$, and $z_{\rm max}$ is the maximum redshift at which the source can be observed at the flux limit of the survey. If $z_{\rm max} > z_{\rm up,\,bin}$, where $z_{\rm up,\,bin}$ is the maximum redshift of the redshift bin, then the $z_{\rm max}$ is the upper boundary of the redshift bin used for computing $V_{\rm max}$. In the case of the ChaMP sample, $z_{\rm max}$ is estimated using both the X-ray and optical survey limits and is selected to be the minimum of the two estimates so the source can be observed at the flux limit of both surveys. We computed the space density using the luminosities derived with $\Gamma = 1.8$. The contribution of sources with photometric redshift to the space density is weighted for the fraction of their $P(z)$ at $z > 3$.

After calculating the $V_{\rm max}$ for each source, we sum the reciprocal values in each redshift bin:

$$\phi = \sum_{i=1}^{z_{\rm min}<z<z_{\rm max}} \left(\frac{1}{V_{{\rm max},i}}\right), \quad (5)$$

where ϕ is the comoving space density in the range $z = z_{\rm min}\ z_{\rm max}$, and i is the index of the sample AGN falling into the redshift bin. The 1σ uncertainty is estimated as

$$\sigma\phi = \sqrt{\sum_{i=1}^{z_{\rm min}<z<z_{\rm max}} \left(\frac{1}{V_{{\rm max},i}}\right)^2}. \quad (6)$$

Including soft, hard, and full band detected sources allows us to compute a space density which takes into account both unobscured sources, which emit more at softer energies, and obscured sources, which emit more at harder energies, without having to introduce any further correction or assumption.

The resulting comoving space densities are shown in Fig. 10. To reduce the effects of incompleteness and to have a complete sample over a given redshift range, we divided the sample in three luminosity intervals (see Fig. 5, shaded areas):

(1) at low luminosities (purple shading), we computed the space density in three redshift bins (z = 3–4.3) at $43.3 < \log(L_{\rm X}/{\rm erg\,s^{-1}}) \leq 44.0$;
(2) at intermediate luminosities (green shading), we computed the space density in three redshift bins (z = 3–5.4) at $44.0 < \log(L_{\rm X}/{\rm erg\,s^{-1}}) \leq 44.7$;
(3) at high luminosities (orange shading), we computed the space density in five redshift bins (z = 3–5.0) at $\log(L_{\rm X}/{\rm erg\,s^{-1}}) > 44.7$.

We also estimated space density upper and lower boundaries by taking into account the X-ray flux errors. If a source has been excluded from the main sample because its flux is lower than the flux limit applied, the same source could be included in the upper boundary sample if its flux+1σ error exceeds the flux limit. Likewise, if a source has been included in the main sample because its flux is higher than the flux limit applied, the same source could be excluded by the lower boundary sample if its flux-1σ error is lower than the flux limit. The shaded areas include the above uncertainties affecting the computation of the space density, i.e. the flux errors and thus errors on the maximum volume associated with each source.

As explained in Section 2.1, the 15 sources with no optical band detection from C-COSMOS survey have not been included in the space density boundaries. However, we computed the space density assuming that all the 15 sources were at the redshift corresponding to the first bin, then to the second bin and so on. The space density values computed in this case, in the first three bins, are within the shaded areas.

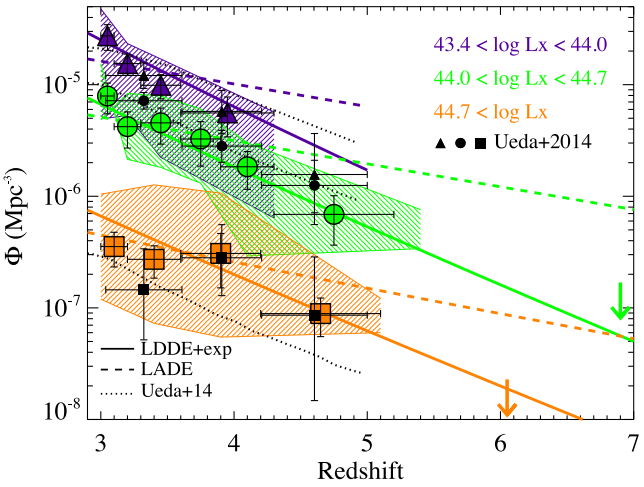

Figure 10. The comoving space density in three different 2–10 keV X-ray luminosity ranges. The solid lines corresponds to the X-ray-selected AGN space density computed for the same luminosity limit from the Gilli et al. (2007) LDDE+exp model. The dashed curve corresponds to the space density derived from the LADE model of Aird et al. (2010). The colours respond to the shaded areas in Fig. 5 and the shaded area represents the maximum and minimum space density under the assumptions described in the text. When only one source is included in the bin it has been plotted as an upper limit (at 3σ). The small black symbols and dotted lines correspond to the comoving space density data points and model derived from Ueda et al. (2014) for similar X-ray luminosity ranges.

The space density in the three luminosity ranges is compared with the predictions, at the same luminosity threshold, from the same three models discussed in Section 4. The LDDE+exp model (Gilli et al. 2007) used for the $\log N$–$\log S$ (solid lines), including in the model all the sources up to a column density of 10^{25} cm^{-2}. We also compare with the LADE model (Aird et al. 2010, dashed line). The LDDE model is fully ruled so it is not included in the following comparisons. In agreement with the results obtained from the number counts, the LDDE+exp model provides an excellent representation of the observed data, although the LADE model cannot be rejected taking into account the upper and lower boundaries. We confirm that the shape of the space density evolution of X-ray-selected luminous AGN is consistent with that derived from optical quasar surveys within current uncertainties.

The results from the Ueda et al. (2014) for AGNs with the same X-ray luminosity ranges are also plotted for comparison (small black symbols). As can be seen, our results are consistent with those of Ueda et al. (2014) within the statistical errors, indicating a significant decline in the AGN space density from $z = 3$ to higher redshifts. To take into account the observed decline in their LDDE model (Fig. 10, black dotted lines), Ueda et al. (2014) introduced another (luminosity-dependent) cutoff redshift above which the model declines. Their model indicates an 'up-sizing' evolution instead of the global 'downsizing' evolution, where more luminous AGNs have their number density peak at higher redshifts compared with less luminous ones. In the cases of lower and intermediate X-ray luminosities, the Ueda et al. (2014) LDDE model slightly overestimates our results but it is within the upper boundaries. In

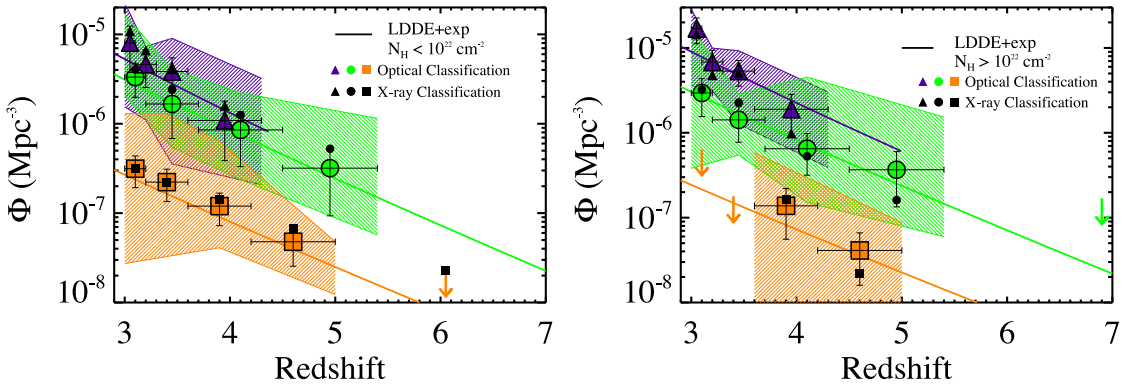

Figure 11. The comoving space density in three different 2–10 keV X-ray luminosity ranges for type-1 (left) and type-2 (right) AGNs. The solid lines corresponds to the X-ray-selected AGN space density computed for the same luminosity limit from the Gilli et al. (2007) model and for $N_{\rm H} \leq 10^{22}$ cm^2 in the case of type-1 AGNs and $N_{\rm H} > 10^{22}$ cm^2 for type-2 AGNs. The colours respond to the shaded areas in Fig. 5 and the shaded area represents the maximum and minimum space density under the assumptions described in Section 5. The small black symbols represent the comoving space density in the three different 2–10 keV X-ray luminosity ranges for sources classified as unobscured (left) and obscured (right) AGNs based on the X-ray classification and the $N_{\rm H} = 10^{22}$ cm^2 limit.

the case of the higher X-ray luminosities, where our data significantly reduce the uncertainties of the Ueda et al. (2014) sample, their model underestimates our result while our data may indicate a flatting up to redshift $z \sim 4$.

5.1 Type-1 versus Type-2 AGNs

Comparing the high-redshift evolution of optical- and X-ray-selected AGN samples, the same decline profile has been revealed. Considering that X-ray-selected samples provide reduced obscuration bias in comparison with optically selected AGN, this similarity suggests no significant cosmological evolution of the obscured AGN fraction at least at higher redshifts. Supporting these result, previous studies have concluded that the obscured AGN fraction increases with redshift $z = 1$ to $z = 2$ (Ballantyne et al. 2006) but decreases at higher redshifts (Hasinger 2008). To investigate further the cosmological evolution of type-1 and type-2 AGNs and their fraction with in the redshift range of $z = 3$–7, we calculate the comoving space density for the two sub-classes of AGNs in our sample following the same method as described in Section 5.

The comoving space density is shown in Fig. 11. The upper and lower boundaries are estimated similarly to Section 5 taking into account the X-ray flux errors and the 15 C-COSMOS source with no optical band detection. We have used both optical (large symbols) and X-ray (small symbols) AGN classification and they seem to be in good agreement. To estimate the upper and lower boundaries, we also take into account the ∼29 per cent of mismatches into the optical and the X-ray classification of AGN types, in order to estimate the upper and lower boundaries. Specifically, in the case of optically classified type-1 AGNs, for the upper boundary we also include in each bin the sources classified as unobscured ($N_{\rm H} < 10^{22}$ cm^{-2}) even if they are defined as type-2 AGNs based on their optical classification. For the lower boundary, we exclude from each bin the type-1 AGNs which have $N_{\rm H} > 10^{22}$ cm^{-2}. The same method is also applied for the type-2 AGNs. So, the upper and lower boundaries include also the uncertainties due to the misclassification of sources.

The space density in the three luminosity ranges is compared with the predictions, at the same luminosity threshold, from the same LDDE+exp Gilli et al. (2007) model, including in the model all the sources with $N_{\rm H} \leq 10^{22}$ cm^{-2} for the case of type-1 AGNs and all the sources with $N_{\rm H} = 10^{22}$–10^{24} cm^{-2} for the case of type-2 AGNs. In agreement with our previous results, the LDDE+exp model provides an excellent representation of both type-1 and type-2 AGNs. Since both type-1 and type-2 AGNs follow the same decline profile it suggests that there is no significant cosmological evolution for their fraction above $z > 3$. The same results are obtained even if we follow the X-ray classification of the AGN sample into obscured and unobscured sources based (Fig. 11, small black symbols).

The LDDE+exp model for these three luminosity ranges and the $N_{\rm H} = 10^{22}$ cm^{-2} division predicts a fraction of objects classified as type-2 over the type-1 AGN sources of 0.63, 0.5, and 0.48 at low luminosities $43.3 < \log(L_{\rm X}/{\rm erg\,s^{-1}}) \leq 44.0$, intermediate luminosities $44.0 < \log(L_{\rm X}/{\rm erg\,s^{-1}}) \leq 44.7$, and high luminosities $\log(L_{\rm X}/{\rm erg\,s^{-1}}) > 44.7$, respectively. For the same luminosity bins, we have calculated the mean comoving space density ratio for the two types $\Phi_{\rm type2}/\Phi_{\rm type1} = 0.59 \pm 0.02, 0.48 \pm 0.04$, and 0.31 ± 0.18 from low to high luminosities. These are in good agreement with the LDDE+exp model predictions.

Recently, Hiroi et al. (2012) estimated the X-ray type-2 AGN fraction, classified based on the $N_{\rm H} > 10^{22}$ cm^{-2} criterion, to be $0.54^{+0.17}_{-0.19}$ at $z = 3.0$–5.0 and in the luminosity range of $\log L_{\rm X} = 44.0$–45.0 while for their optical selection of type-2 AGNs they found a fraction of 0.59 ± 0.09. Their estimates are somewhat larger than our result of 0.48 ± 0.04, although they agree within the errors. This difference could be easily explained from the fact that their sample is significantly smaller (30 sources) than ours and contains only four sources with $z > 4$ from which the two classified as type-2 AGN have only photometric redshifts.

6 SUMMARY

We have presented the results of the largest X-ray-selected sample of $z > 3$ AGNs to date, compiled from the C-COSMOS and ChaMP surveys. The large body of C-COSMOS and ChaMP data and their combination allowed us to devise a robust method to build a sizeable sample of X-ray-selected AGNs and control the selection effects including both type-1 (unobscured) and type-2 (obscured) AGNs, at $z > 3$. Our sample consists of 209 detections in the soft and/or hard and/or full band. We find:

(1) The average HR of the type-1 and type-2 AGN samples is consistent with the $N_{\rm H} < 10^{22}$ cm^{-2} criterion for the

classification of the X-ray unobscured AGNs and the $N_{\rm H} > 10^{22}\,{\rm cm}^{-2}$ criterion for the classification of the X-ray obscured AGNs, respectively.

(2) For the individual sources, there is a mismatch of ∼26 per cent between optical and X-ray classification. The contribution from starburst emission in the soft band, or misclassification of faint type-1 with strong optical/IR contamination from host galaxy light could possibly explain the differences between the two classifications.

(3) The number counts derived in this work (Fig. 9) are consistent with previous determinations from the literature, yet significantly reduce the uncertainties especially at bright fluxes and at high redshifts ($z > 4$). The number counts of our combined C-COSMOS/ChaMP sources are consistent with the trend that the space density significantly declines at higher redshifts, similarly to XMM (Brusa et al. 2009) and *Chandra* (Civano et al. 2011) COSMOS results at similar fluxes at least within their errors and CDF-S (Vito et al. 2013) at fainter fluxes, and are better described by the LDDE+exp model (Gilli et al. 2007).

In contrast to the previous studies, and due mainly to the large sample and wide flux coverage, our results exclude the Aird et al. (2010) LADE model, at the brighter fluxes. At fluxes $2 \times 10^{-16} \leq F_{0.5\text{–}2\,{\rm keV}} \leq 2 \times 10^{-15}\,{\rm erg\,cm^{-2}\,s^{-1}}$, the predictions of this model are very similar to the Gilli et al. (2007) LDDE+exp model, but at fainter and brighter fluxes the two models deviate significantly. The Vito et al. (2013) results trace the Gilli et al. (2007) LDDE+exp model well at fainter fluxes, but only for $z > 3$, while our sample give the same results at the brighter fluxes where (due to the low expected counts) a large sample is required.

(4) In agreement with the number counts, the space density is well described with the LDDE+exp model at all X-ray luminosity bins and redshifts, while the LADE model fails to fit the data. These results confirm the declining space density as observed in the optical wavelengths.

(5) Taking into account both optical and X-ray classifications, we derived the space density for type-1 and type-2 (obscured and unobscured) AGNs separately. In both cases, the results are in agreement with the LDDE+exp model suggesting that the high-redshift evolution of obscured AGNs is similar to that of unobscured AGNs. For each luminosity bin, we derived the type-2 AGN fraction among the total AGN sample to be 0.59 ± 0.02, 0.48 ± 0.04, and 0.31 ± 0.18 at $z > 3$ in the luminosity ranges of $L_{\rm X} = 10^{43.3\text{–}44.0}$, $10^{44.0\text{–}44.7}$, and $10^{44.7\text{–}46.0}\,{\rm erg\,s^{-1}}$.

The last result should have a significant impact on our understanding of the galaxy and black hole co-evolution. Either or both line-of-sight orientation or evolutionary phase (e.g. covering factor of high column obscuration) can affect the apparent obscuration (and therefore classification) of AGNs. Given that orientation does not evolve preferentially towards us, this work allows us to say that the obscured and unobscured evolutionary phases do evolve similarly.

ACKNOWLEDGEMENTS

The authors thank J. Aird and E. Glikman for sharing their luminosity functions and Y. Ueda for providing his space density estimations. The authors would like to thank the referee F. Bauer for the helpful and constructive report. This work was supported by NASA Chandra archival grant, designated code 617817 and contract number AR2-13010X.

REFERENCES

Aird J. et al., 2010, MNRAS, 401, 2531
Alexander D. M., Brandt W. N., Hornschemeier A. E., Garmire G. P., Schneider D. P., Bauer F. E., Griffiths R. E., 2001, AJ, 122, 2156
Alexandroff R. et al., 2013, MNRAS, 435, 3306
Antonucci R., 1993, ARA&A, 31, 473
Arnouts S., Ilbert O., 2011, Astrophysics Source Code Library, Record ascl:1108.009, 8009
Ballantyne D. R., 2008, ApJ, 685, 787
Ballantyne D. R., Everett J. E., Murray N., 2006, ApJ, 639, 740
Barger A. J., Cowie L. L., 2005, ApJ, 635, 115
Brandt W. N., Hasinger G., 2005, ARA&A, 43, 827
Brusa M. et al., 2003, A&A, 409, 65
Brusa M. et al., 2009, ApJ, 693, 8
Brusa M. et al., 2010, ApJ, 716, 348
Burlon D., Ajello M., Greiner J., Comastri A., Merloni A., Gehrels N., 2011, ApJ, 728, 58
Cappelluti N. et al., 2009, A&A, 497, 635
Casali M. et al., 2007, A&A, 467, 777
Civano F., Comastri A., Brusa M., 2005, MNRAS, 358, 693
Civano F. et al., 2011, ApJ, 741, 91
Civano F. et al., 2012, ApJS, 201, 30
Comastri A., Brunetti G., Dallacasa D., Bondi M., Pedani M., Setti G., 2003, MNRAS, 340, L52
Cowie L. L., Songaila A., Hu E. M., Cohen J. G., 1996, AJ, 112, 839
Croton D. J. et al., 2006, MNRAS, 365, 11
Damen M., Labbé I., Franx M., van Dokkum P. G., Taylor E. N., Gawiser E. J., 2009, ApJ, 690, 937
Draper A. R., Ballantyne D. R., 2010, ApJ, 715, L99
Dye S. et al., 2006, MNRAS, 372, 1227
Elvis M. et al., 2009, ApJS, 184, 158
Fan X. et al., 2001, AJ, 121, 54
Ferrarese L., Merritt D., 2000, ApJ, 539, L9
Fiore F. et al., 2003, A&A, 409, 79
Freeman P., Doe S., Siemiginowska A., 2001, in Starck J.-L., Murtagh F. D., eds, SPIE Conf. Ser. Vol. 4477, Astronomical Data Analysis. SPIE, Bellingham, p. 76
Garmire G. P., Bautz M. W., Ford P. G., Nousek J. A., Ricker G. R., Jr, 2003, in Truemper J. E., Tananbaum H. D., eds, SPIE Conf. Ser. Vol. 4851, X-Ray and Gamma-Ray Telescopes and Instruments for Astronomy. SPIE, Bellingham, p. 28
Gebhardt K. et al., 2000, ApJ, 539, L13
Gilli R., Comastri A., Hasinger G., 2007, A&A, 463, 79
Glikman E., Djorgovski S. G., Stern D., Dey A., Jannuzi B. T., Lee K.-S., 2011, ApJ, 728, L26
Granato G. L., Silva L., Monaco P., Panuzzo P., Salucci P., De Zotti G., Danese L., 2001, MNRAS, 324, 757
Granato G. L., De Zotti G., Silva L., Bressan A., Danese L., 2004, ApJ, 600, 580
Green P. J. et al., 2009, ApJ, 690, 644
Hambly N. C. et al., 2008, MNRAS, 384, 637
Hasinger G., 2008, A&A, 490, 905
Hasinger G. et al., 2001, A&A, 365, L45
Hasinger G., Miyaji T., Schmidt M., 2005, A&A, 441, 417
Hewett P. C., Warren S. J., Leggett S. K., Hodgkin S. T., 2006, MNRAS, 367, 454
Hiroi K., Ueda Y., Akiyama M., Watson M. G., 2012, ApJ, 758, 49
Hodgkin S. T., Irwin M. J., Hewett P. C., Warren S. J., 2009, MNRAS, 394, 675
Hopkins P. F., Somerville R. S., Hernquist L., Cox T. J., Robertson B., Li Y., 2006, ApJ, 652, 864
Ikeda H. et al., 2011, ApJ, 728, L25
Ilbert O. et al., 2009, ApJ, 690, 1236
Jiang L., Fan X., Vestergaard M., Kurk J. D., Walter F., Kelly B. C., Strauss M. A., 2007, AJ, 134, 1150
Jiang L. et al., 2009, AJ, 138, 305

Kalfountzou E., Trichas M., Rowan-Robinson M., Clements D., Babbedge T., Seiradakis J. H., 2011, MNRAS, 413, 249
Kalfountzou E., Jarvis M. J., Bonfield D. G., Hardcastle M. J., 2012, MNRAS, 427, 2401
Kalfountzou E. et al., 2014, MNRAS, 442, 1181
Kim M. et al., 2007, ApJS, 169, 401
Kodama T. et al., 2004, MNRAS, 350, 1005
Koekemoer A. M. et al., 2004, ApJ, 600, L123
La Franca F. et al., 2005, ApJ, 635, 864
Laird E. S. et al., 2009, ApJS, 180, 102
Lanzuisi G. et al., 2013, MNRAS, 431, 978
Lawrence A., Elvis M., 1982, ApJ, 256, 410
Lawrence A., Elvis M., 2010, ApJ, 714, 561
Lawrence A. et al., 2007, MNRAS, 379, 1599
Lehmann I. et al., 2001, A&A, 371, 833
Lilly S. J. et al., 2007, ApJS, 172, 70
Lilly S. J. et al., 2009, ApJS, 184, 218
Maccacaro T., Gioia I. M., Wolter A., Zamorani G., Stocke J. T., 1988, ApJ, 326, 680
Maddox N., Hewett P. C., Warren S. J., Croom S. M., 2008, MNRAS, 386, 1605
Magorrian J. et al., 1998, AJ, 115, 2285
McConnell N. J., Ma C.-P., 2013, ApJ, 764, 184
Menci N., Fiore F., Puccetti S., Cavaliere A., 2008, ApJ, 686, 219
Merloni A. et al., 2014, MNRAS, 437, 3550
Nandra K., Pounds K. A., 1994, MNRAS, 268, 405
Noterdaeme P. et al., 2012, A&A, 547, L1
Osterbrock D. E., Koski A. T., 1976, MNRAS, 176, 61P
Pâris I. et al., 2014, A&A, 563, A54
Park T., Kashyap V. L., Siemiginowska A., van Dyk D. A., Zezas A., Heinke C., Wargelin B. J., 2006, ApJ, 652, 610
Puccetti S. et al., 2009, ApJS, 185, 586
Richards G. T. et al., 2002, AJ, 123, 2945
Richards G. T. et al., 2006, AJ, 131, 2766
Richards G. T. et al., 2009, ApJS, 180, 67
Ross N. P. et al., 2013, ApJ, 773, 14
Ruiz A., Miniutti G., Panessa F., Carrera F. J., 2010, A&A, 515, A99
Salvato M. et al., 2009, ApJ, 690, 1250
Salvato M. et al., 2011, ApJ, 742, 61
Schmidt M., 1968, ApJ, 151, 393
Schmidt M., Schneider D. P., Gunn J. E., 1995, AJ, 110, 68
Schmidt M. et al., 1998, A&A, 329, 495
Silverman J. D. et al., 2008, ApJ, 679, 118
Silverman J. D. et al., 2010, ApJS, 191, 124
Spergel D. N. et al., 2003, ApJS, 148, 175
Steidel C. C., Giavalisco M., Pettini M., Dickinson M., Adelberger K. L., 1996, ApJ, 462, L17
Stern J., Laor A., 2012, MNRAS, 426, 2703
Stocke J. T., Morris S. L., Gioia I. M., Maccacaro T., Schild R., Wolter A., Fleming T. A., Henry J. P., 1991, ApJS, 76, 813
Treister E., Urry C. M., 2006, ApJ, 652, L79
Treister E., Urry C. M., Virani S., 2009, ApJ, 696, 110
Trichas M., Georgakakis A., Rowan-Robinson M., Nandra K., Clements D., Vaccari M., 2009, MNRAS, 399, 663
Trichas M. et al., 2010, MNRAS, 405, 2243
Trichas M. et al., 2012, ApJS, 200, 17
Trichas M. et al., 2013, ApJ, 778, 188
Ueda Y., Akiyama M., Ohta K., Miyaji T., 2003, ApJ, 598, 886
Ueda Y., Akiyama M., Hasinger G., Miyaji T., Watson M. G., 2014, ApJ, 786, 104
Urry C. M., Padovani P., 1995, PASP, 107, 803
Vignali C., Brandt W. N., Schneider D. P., 2003, AJ, 125, 433
Vito F. et al., 2013, MNRAS, 428, 354
Warren S. J., Hewett P. C., Foltz C. B., 2000, MNRAS, 312, 827
Weisskopf M. C., Brinkman B., Canizares C., Garmire G., Murray S., Van Speybroeck L. P., PASP, 114, 1
Willott C. J. et al., 2010, AJ, 139, 906
Wright E. L. et al., 2010, AJ, 140, 1868
Wu X.-B., Jia Z., 2010, MNRAS, 406, 1583
Wu X.-B., Zhang W., Zhou X., 2004, ChjAA, 4, 17
Wu X.-B., Hao G., Jia Z., Zhang Y., Peng N., 2012, AJ, 144, 49
Xue Y. Q. et al., 2011, ApJS, 195, 10
Young M., Elvis M., Risaliti G., 2010, ApJ, 708, 1388

APPENDIX A

QSO candidates at redshift $\simeq$3.0–3.5 satisfied the following cuts:

$$\begin{aligned} \sigma_r &< 0.13 && \text{AND} \\ u &> 20.6 && \text{AND} \\ u-g &> 1.5 && \text{AND} \\ g-r &< 1.2 && \text{AND} \\ r-i &< 0.3 && \text{AND} \\ i-z &> -1.0 && \text{AND} \\ g-r &< 0.44(u-g)-0.76. \end{aligned} \tag{A1}$$

For the redshift range $\simeq$3.5–4.5, this selection becomes

$$\begin{aligned} &\text{(A)} \quad \sigma_r < 0.2 \\ &\text{(B)} \quad u-g > 1.5 \quad \text{OR} \quad u > 20.6 \\ &\text{(C)} \quad g-r > 0.7 \\ &\text{(D)} \quad g-r > 2.8 \quad \text{OR} \quad r-i < 0.44(g-r)-0.558 \\ &\text{(E)} \quad i-z < 0.25 \ \text{AND} \ i-z > -1.0, \end{aligned} \tag{A2}$$

in the combination A AND B AND C AND D AND E. For the redshifts above $\simeq$4.5, we use

$$\begin{aligned} u &> 21.5 && \text{AND} \\ g &> 21.0 && \text{AND} \\ r-i &> 0.6 && \text{AND} \\ i-z &> -1.0 && \text{AND} \\ i-z &< 0.52(r-i)-0.762. \end{aligned} \tag{A3}$$

Table A1. Properties of the high-redshift AGN sample.

Survey[a]	RA (deg)	Dec. (deg)	z_{spec}	z_{phot}	z_{phot}[b] lower	z_{phot}[c] upper	Optical type[h]	X-ray type[i]	S_{soft}[d]	logLx[e]	HR[f]	HR low[j]	HR up[k]	N_H[g]
1	1.682	−0.200	3.109	–	–	–	1	1	0.071	44.65	−0.50	−0.77	−0.12	0.1
1	5.826	−1.048	–	4.5	4.3	4.7	1	1	0.094	45.13	–	–	−0.38	<1.0
1	18.1925	−1.2188	3.592	3.545	3.35	4.37	1	1	0.090	44.90	−0.84	−0.98	−0.57	<0.1
1	29.8140	0.4529	–	3.675	3.51	4.05	1	1	0.039	44.56	−0.92	–	−0.84	<0.1
1	29.886	0.482	–	4.6	4.3	4.9	2	1	0.037	44.75	−0.70	–	−0.53	<0.1
1	32.680	−0.3051	4.733	4.565	4.05	4.98	1	1	0.277	45.65	−0.67	−0.85	−0.56	<0.1
1	38.906	−0.722	–	4.15	3.72	4.58	2	1	0.203	45.39	−0.58	−0.76	−0.41	<0.1
1	116.8620	27.6253	3.152	2.905	2.58	3.25	1	1	0.072	44.67	−0.42	−0.70	−0.09	0.1
1	119.1940	41.1201	3.734	3.135	2.88	4.29	1	1	0.130	45.09	−0.41	−0.66	−0.14	0.1
1	119.218	45.044	3.185	–	–	–	1	1	0.105	44.85	−0.85	−0.98	−0.62	<0.1
1	120.2877	36.1514	–	3.675	3.59	4.06	1	1	0.156	45.16	−0.64	−0.69	−0.56	<0.1
1	125.4118	12.2922	3.112	–	–	–	1	1	0.053	44.53	−0.64	−0.76	−0.47	<0.1
1	125.4123	12.2917	3.114	2.995	2.78	3.23	1	1	0.443	45.45	−0.48	−0.51	−0.42	<0.1
1	127.837	19.151	–	4.6	4.2	5.0	2	1	0.065	44.99	−0.57	−0.73	−0.42	<0.1
1	130.2606	13.2202	–	2.945	2.76	3.29	1	1	0.078	44.66	−0.54	−0.66	−0.44	<0.1
1	132.169	44.959	3.093	–	–	–	1	1	0.030	44.28	−0.31	−0.41	−0.22	4.0
1	133.446	57.987	–	4.1	3.4	4.8	2	1	0.043	44.70	−0.36	−0.55	−0.19	4.0
1	134.4131	9.0255	3.130	3.065	2.76	3.39	1	1	0.076	44.69	−0.57	−0.89	−0.05	0.1
1	137.6868	17.7420	4.098	4.105	3.35	4.47	1	1	0.044	44.71	−0.50	−0.67	−0.35	0.1
1	137.786	54.298	3.234	–	–	–	2	1	0.036	44.40	−0.44	−0.55	−0.35	0.1
1	138.0425	5.7952	3.246	3.345	3.09	3.63	1	1	0.065	44.64	−0.50	−0.70	−0.29	0.1
1	139.086	29.522	3.098	–	–	–	1	1	0.054	44.53	−0.40	−0.57	−0.19	0.1
1	141.0521	31.2774	–	2.795	2.21	3.03	1	1	0.367	45.34	−0.65	−0.79	−0.48	<0.1
1	143.3646	55.4032	–	3.045	2.78	3.33	1	1	0.086	44.72	−0.31	−0.43	−0.20	4.0
1	149.425	33.251	3.001	–	–	–	1	1	0.128	44.87	−0.77	−0.93	−0.49	<0.1
1	149.5942	7.7968	3.220	3.145	2.8	3.47	1	1	0.086	44.77	–	–	−0.88	<0.1
1	150.7009	32.7668	–	3.405	3.11	4.37	1	1	0.085	44.82	−0.45	−0.61	−0.34	0.1
1	155.4521	13.1647	3.055	2.905	2.55	3.26	1	1	0.075	44.66	−0.47	−0.67	−0.21	0.1
1	156.5952	47.3187	4.941	4.895	4.77	5.1	1	1	0.102	45.25	−0.44	−0.90	−0.24	0.1
1	162.590	58.625	–	3.65	3.47	3.83	2	1	0.077	44.84	−0.56	−0.82	−0.22	0.1
1	162.938	57.468	3.409	–	–	–	1	1	0.051	44.60	−0.99	−1.0	−0.73	<0.1
1	163.275	57.5735	–	2.755	2.52	3.1	1	1	0.045	44.44	−0.75	−0.87	−0.59	<0.1
1	168.5505	40.5661	3.597	3.495	3.09	4.35	1	1	0.053	44.67	−0.44	−0.6	−0.32	0.1
1	168.7335	40.6372	4.913	1.305	0.9	1.52	2	1	0.253	45.64	−0.69	−0.73	−0.64	<0.1
1	169.4807	48.0722	–	2.905	2.54	3.23	1	1	0.101	44.84	−0.68	−0.77	−0.57	<0.1
1	169.607	7.7262	–	3.75	3.45	4.05	1	2	0.035	44.53	−0.24	−0.41	−0.09	13.0
1	170.0871	43.4292	3.552	3.665	2.92	4.12	1	1	0.073	44.79	−0.46	−0.61	−0.32	0.1
1	170.5414	24.2938	3.336	3.045	2.73	3.39	1	1	0.054	44.61	−0.51	−0.66	−0.38	0.1
1	171.748	56.772	–	3.6	3.5	3.7	1	1	0.033	44.46	−0.77	−0.96	−0.53	<0.1
1	175.151	66.221	3.337	–	–	–	1	1	0.065	44.68	−0.67	−0.74	−0.61	<0.1
1	178.8811	−1.770	3.202	3.495	3.16	4.21	1	1	0.055	44.57	−0.35	−0.47	−0.21	2.0
1	182.037	0.129	–	3.5	2.4	4.6	2	2	0.056	44.66	−0.17	−0.44	0.08	17.0
1	183.2733	2.8584	–	3.145	2.76	3.83	1	1	0.165	45.11	−0.64	−0.71	−0.53	<0.1
1	183.366	2.960	–	3.5	2.4	4.6	1	1	0.090	44.87	−0.46	−0.65	−0.24	0.1
1	188.1259	47.6153	3.041	3.205	2.88	3.83	1	1	0.175	45.02	−0.99	−0.99	−0.76	<0.1
1	190.4594	9.6307	–	3.045	2.66	3.37	2	2	0.057	44.54	−0.18	−0.44	0.04	13.0
1	192.551	33.855	3.6	–	–	–	1	1	0.074	44.81	−0.54	−0.83	−0.35	0.1
1	192.9299	0.1240	–	2.905	2.69	3.23	1	1	0.220	45.38	−0.5	−0.68	−0.27	0.1
1	195.0080	1.3067	4.612	4.485	3.88	4.69	1	1	0.454	45.84	−0.37	−0.73	−0.02	4.0
1	195.445	−0.112	3.7	–	–	–	1	2	0.160	45.17	−0.16	−0.41	0.09	20.0
1	196.534	3.940	6.016	–	–	–	1	1	0.031	44.93	−0.69	−0.75	−0.61	<0.1
1	196.6521	46.4961	–	3.065	2.76	3.23	2	1	0.055	44.53	−0.26	−0.53	0.06	8.0
1	197.4348	57.6389	–	2.905	2.67	3.25	1	1	0.068	44.69	–	–	−0.64	<0.1
1	198.2170	42.4716	3.181	2.945	2.75	3.3	1	1	0.072	44.81	−0.66	−0.82	−0.52	<0.1
1	199.322	1.1538	–	3.4	3.275	3.525	1	1	0.090	44.84	−0.59	−0.94	−0.20	0.1
1	201.424	11.477	–	4.6	4.3	4.9	2	2	0.071	45.03	0.01	−0.33	0.4	50.0
1	201.8283	29.1482	–	3.675	3.6	4.08	1	1	0.030	44.45	−0.97	−0.99	−0.53	<0.1
1	202.9168	11.2840	–	2.755	2.21	3.03	1	1	0.057	44.53	−0.56	−0.68	−0.40	<0.1
1	203.5933	−1.4221	3.827	3.775	3.01	4.33	1	1	0.032	44.51	−0.51	−0.90	−0.34	0.1
1	203.6122	−1.4816	–	2.905	2.57	3.26	1	1	0.074	44.69	−0.66	−0.94	−0.54	<0.1
1	206.078	−0.511	3.070	–	–	–	1	1	0.060	44.57	−0.64	−0.84	−0.51	<0.1
1	207.7399	60.1377	–	3.285	3.05	3.95	1	1	0.110	44.89	−0.68	−0.75	−0.63	<0.11

Table A1 – *continued*

Survey[a]	RA (deg)	Dec. (deg)	z_{spec}	z_{phot}	z_{phot}[b] lower	z_{phot}[c] upper	Optical type[h]	X-ray type[i]	S_{soft}[d]	logLx[e]	HR[f]	HR low[j]	HR up[k]	N_H[g]
1	208.2111	33.4822	–	2.755	2.32	3.07	1	1	0.056	44.54	−0.462	−0.57	−0.30	0.1
1	212.7671	52.2988	–	2.815	2.66	3.13	1	1	0.097	44.99	−0.42	−0.48	−0.36	0.1
1	214.2243	44.6294	–	2.795	2.52	3.12	1	1	0.134	44.94	−0.54	−0.66	−0.43	<0.1
1	214.4241	53.0886	–	3.495	3.15	4.37	1	1	0.037	44.49	−0.75	−0.85	−0.61	<0.1
1	214.8523	53.5323	–	3.535	3.41	3.9	1	1	0.185	45.20	−0.74	−0.95	−0.47	<0.1
1	215.1504	47.2415	3.237	2.905	2.71	3.26	1	1	0.300	45.32	−0.75	−0.90	−0.58	<0.1
1	215.7710	24.0856	4.112	4.165	3.36	4.54	1	2	0.032	44.58	−0.26	−0.54	0.01	14.0
1	216.0719	22.8406	–	3.675	3.58	4.06	1	1	0.734	45.83	−0.60	−0.64	−0.56	<0.1
1	216.447	35.455	3.53	–	–	–	1	1	0.053	44.65	−0.56	−0.66	−0.41	<0.1
1	218.114	−1.160	–	3.3	3.0	3.6	2	1	0.079	44.76	−0.41	−0.56	−0.28	0.1
1	219.5024	3.6388	3.306	3.285	2.92	4.08	1	1	0.058	44.62	−0.58	−0.68	−0.48	<0.1
1	219.633	3.641	–	3.275	3.05	3.5	1	1	0.070	44.70	−0.81	−0.89	−0.72	<0.1
1	219.6653	3.6288	3.194	3.205	2.88	3.94	1	1	0.040	44.44	−0.68	−0.77	−0.56	<0.1
1	220.8577	58.8995	–	2.905	2.68	3.22	1	1	0.030	44.32	−0.84	−0.96	−0.35	0.1
1	221.3084	−0.4237	3.142	3.065	2.68	3.36	1	1	0.058	44.58	−0.24	−0.54	0.0	10.0
1	225.0836	22.7196	3.268	3.475	3.18	4.21	1	1	0.051	44.56	−0.79	−0.97	−0.41	<0.1
1	230.1945	52.9896	3.385	3.495	3.15	4.35	1	1	0.060	44.66	−0.63	−0.83	−0.34	<0.1
1	230.8973	28.6609	–	2.715	2.44	3.02	1	1	0.062	44.56	−0.61	−0.72	−0.48	<0.1
1	240.6529	42.5518	3.889	4.125	3.27	4.46	1	1	0.045	44.72	−0.82	−1.0	−0.71	<0.1
1	244.0288	47.2661	–	3.205	2.92	3.97	1	1	0.058	44.60	−0.58	−0.95	0.01	0.1
1	258.2694	61.3793	3.150	3.005	2.76	3.33	1	1	0.126	44.91	–	–	−0.89	<0.1
1	258.956	63.246	–	3.6	3.5	3.7	1	1	0.139	45.09	−0.61	−0.86	−0.27	<0.1
1	260.0728	26.5628	3.057	3.145	2.77	3.5	1	1	0.053	44.51	−0.85	−0.95	−0.71	<0.1
1	340.9458	−9.6855	–	4.125	3.36	4.56	1	1	0.078	44.97	−0.71	−0.88	−0.48	<0.1
1	359.3544	0.6643	–	3.285	2.98	4.19	1	1	0.039	44.45	–	–	−0.75	<0.1
2	149.5438	1.9537	–	2.951	2.91	3.01	2	2	0.024	44.28	0.49	0.32	0.79	80.0
2	149.6242	1.8854	–	2.264	2.1	3.86	1	1	0.007	43.98	–	–	−0.34	<3.0
2	149.6908	2.2641	–	–	>3.0	–	–	2	0.031	45.46	0.22	−0.17	0.53	50.0
2	149.6696	2.1677	3.089	3.094	2.75	3.21	2	2	0.018	44.21	−0.04	−0.18	0.10	22.0
2	149.7362	2.1799	4.255	4.245	4.23	4.26	1	1	0.014	44.40	−0.41	−0.59	−0.23	0.1
2	149.7425	2.5354	–	2.942	2.9	3.01	2	2	−0.015	44.30	–	0.31	–	≥55.0
2	149.7617	2.4358	–	3.647	3.64	3.66	1	2	0.023	44.46	−0.16	−0.39	−0.11	22.0
2	149.7710	2.3658	–	3.447	3.35	3.53	2	2	0.002	43.38	–	–	0.73	<1000.0
2	149.7821	2.4713	–	3.246	3.23	3.26	1	2	−0.014	44.334	–	−0.05	–	≥25.0
2	149.7837	2.4521	5.07	1.939	1.9	1.98	2	2	0.007	44.31	–	–	0.11	<75.0
2	149.7975	2.2897	–	–	>3.0	–	–	2	−0.002	44.33	–	0.69	–	<1000.0
2	149.8035	2.1417	–	2.838	2.24	3.09	1	2	0.009	43.87	−0.37	−0.58	−0.12	1.5
2	149.8046	2.1189	–	3.791	1.59	4.58	2	2	0.004	43.68	–	–	0.60	<300.0
2	149.8079	1.8105	–	2.382	2.33	3.260	1	2	0.006	43.79	−0.22	−0.65	0.20	11.0
2	149.8085	2.3148	–	3.471	3.41	3.79	2	1	0.025	44.44	−0.34	−0.46	−0.23	4.0
2	149.8123	2.2830	–	3.297	3.24	3.35	1	1	0.009	43.95	–	–	−0.69	0.1
2	149.8144	2.7348	–	–	>3.0	–	–	2	0.021	45.29	–	–	0.51	<85
2	149.8233	2.5398	–	–	>3.0	–	–	2	−0.010	44.97	–	0.52	–	>85
2	149.8458	2.4817	–	3.375	3.36	3.39	1	1	0.007	43.87	–	–	−0.498	<0.1
2	149.8515	2.2764	3.371	3.317	3.3	3.33	1	1	0.012	44.09	−0.53	−0.70	−0.35	0.1
2	149.8517	2.4269	–	3.35	3.16	3.58	2	2	0.004	43.69	0.33	0.15	0.52	68.0
2	149.8585	2.4093	–	4.108	3.68	4.29	2	2	0.049	44.91	−0.27	−0.34	−0.21	11.0
2	149.8605	2.3876	–	2.949	2.33	3.97	1	2	0.002	43.51	0.22	−0.13	0.57	65.0
2	149.8697	2.2941	3.345	3.4	3.39	3.41	1	2	0.024	44.42	0.06	−0.02	0.15	37.0
2	149.8744	2.3615	–	6.88	6.88	7.0	2	2	0.002	44.10	–	–	0.74	<1000.0
2	149.8792	2.2258	3.65	3.647	3.64	3.66	1	1	0.018	44.35	−0.41	−0.54	−0.28	0.1
2	149.8825	2.5051	–	3.1	3.02	3.19	2	2	0.046	44.60	−0.22	−0.29	−0.16	10.0
2	149.8861	2.2759	3.335	3.277	3.26	3.3	2	2	−0.004	43.83	–	0.29	–	>65.0
2	149.8894	1.9662	–	3.053	2.2	3.12	2	1	0.004	43.47	–	–	−0.32	<5.0
2	149.8942	2.4330	3.382	3.393	3.38	3.41	1	2	0.003	43.43	−0.19	−0.70	0.31	14.0
2	149.8977	2.3244	–	2.998	2.9	3.16	2	2	0.006	43.72	–	–	0.45	<75.0
2	149.9084	2.5723	–	–	>3.0	–	–	2	0.004	43.64	–	–	0.88	<1000.0
2	149.9093	2.6199	–	2.569	2.13	4.23	1	1	0.006	44.02	–	–	−0.29	<6.0
2	149.9108	1.8996	–	3.063	2.585	3.194	2	2	0.002	43.24	–	–	0.62	<200.0
2	149.9111	1.8427	–	3.295	2.81	3.45	2	–	−0.003	43.50	–	–	–	–
2	149.9137	2.2465	–	–	>3.0	–	–	2	0.010	44.02	0.46	0.23	0.52	71.0
2	149.9195	2.3454	3.021	3.043	3.03	3.05	1	1	0.009	43.85	–	–	−0.69	<0.1
2	149.9249	1.8441	–	2.936	1.79	3.05	2	2	0.004	43.55	–	–	−0.21	<13.0

Table A1 – *continued*

Survey[a]	RA (deg)	Dec. (deg)	z_{spec}	z_{phot}	z_{phot}[b] lower	z_{phot}[c] upper	Optical type[h]	X-ray type[i]	S_{soft}[d]	logLx[e]	HR[f]	HR low[j]	HR up[k]	N_H[g]
2	149.9316	2.3519	–	–	>3.0	–	–	2	0.004	43.62	–	0.87	–	1000.0
2	149.9445	1.7404	–	2.044	2.0	3.66	1	1	0.006	43.88	–	–	−0.28	<6.0
2	149.9522	2.6514	3.08	3.083	3.07	3.09	2	2	−0.011	44.16	–	0.411	–	>70.0
2	149.9666	2.4325	–	2.893	2.23	3.3	2	2	−0.013	44.33	–	0.753	–	>1000.0
2	149.9692	2.3048	3.155	3.099	3.076	3.13	1	2	0.014	44.12	0.06	−0.07	0.19	32.0
2	149.9728	1.9415	–	2.843	2.63	3.06	2	1	0.013	44.02	−0.26	−0.41	−0.12	7.0
2	149.9816	2.3150	–	3.003	2.97	3.03	2	2	0.023	44.28	−0.06	−0.15	0.04	22.0
2	149.9905	2.2973	3.026	2.97	2.93	3.05	2	1	0.009	43.87	–	–	−0.72	<0.1
2	149.9986	1.9745	–	2.911	2.88	3.01	2	1	0.013	44.02	–	–	−0.78	<0.1
2	150.0044	2.0389	3.515	3.5	3.49	3.51	1	1	0.018	44.31	−0.41	−0.54	−0.28	0.1
2	150.0070	1.9180	–	–	>3.0	–	–	2	0.006	43.76	0.60	0.33	0.78	150.0
2	150.0078	2.1489	–	2.851	2.77	3.43	1	2	0.005	43.78	0.17	−0.03	0.37	48.0
2	150.0094	1.8526	–	4.032	4.02	4.05	2	1	0.008	44.11	–	–	−0.63	<0.1
2	150.0172	2.4979	–	2.914	2.5	3.26	2	1	0.009	43.95	–	–	−0.71	<0.1
2	150.0258	2.0038	–	3.124	2.67	3.17	2	2	−0.006	43.93	–	0.48	–	≥1000.0
2	150.0427	1.8722	3.371	3.338	3.32	3.35	1	2	0.008	43.94	−0.32	−0.58	−0.06	5.0
2	150.0465	2.3674	–	2.313	1.94	3.1	2	1	0.004	43.50	–	–	−0.39	0.1
2	150.0483	2.4816	–	–	>3.0	–	–	2	0.004	43.64	–	–	0.86	1000.0
2	150.0621	1.7226	–	3.033	2.91	3.41	2	2	0.008	43.84	0.06	−0.21	0.33	32.0
2	150.0635	2.4219	–	3.087	3.02	3.25	2	2	−0.006	43.93	–	0.48	–	>80.0
2	150.0637	1.7774	–	3.426	1.21	3.84	2	2	−0.009	44.17	–	0.32	–	>50.0
2	150.0647	2.1910	–	2.887	1.53	3.06	1	2	0.025	44.35	0.11	0.03	0.19	35.0
2	150.0673	2.0843	–	3.01	2.99	3.03	1	1	0.006	43.66	–	–	−0.57	<0.1
2	150.0862	2.139	–	5.045	4.73	5.14	1	2	0.003	43.99	0.25	0.01	0.49	100.0
2	150.0910	1.9292	–	2.864	2.84	3.23	1	2	−0.007	44.04	–	0.54	–	>90.0
2	150.0969	2.0215	3.546	3.362	3.33	3.39	2	1	0.006	43.81	–	–	−0.59	<0.1
2	150.0999	2.1527	–	2.844	2.6	3.06	2	1	0.008	43.81	–	–	−0.67	<0.1
2	150.1010	2.4194	4.66	4.545	4.53	4.56	1	2	0.009	44.33	−0.27	−0.49	−0.05	14.0
2	150.1074	1.7592	4.16	3.949	3.93	3.96	1	2	0.006	44.01	0.01	−0.28	0.3	43.0
2	150.1336	2.4574	3.189	3.111	3.08	3.15	2	1	0.006	43.71	–	–	−0.494	<0.1
2	150.1522	2.3079	3.175	3.163	3.08	3.24	2	2	0.003	43.55	0.42	0.24	0.60	75.0
2	150.1640	2.1793	–	2.82	2.75	3.15	1	2	−0.004	43.57	–	0.407	–	27.0
2	150.1763	2.5697	–	3.144	3.09	3.24	2	2	0.005	43.61	–	–	0.65	<5000.0
2	150.1807	2.0760	3.01	3.015	3.0	3.03	1	1	0.011	43.94	–	–	−0.77	<0.1
2	150.1926	2.2199	3.09	3.077	3.07	3.09	1	2	0.007	43.76	−0.15	−0.39	0.1	15.0
2	150.1997	1.7312	–	2.821	2.66	3.45	2	2	0.004	43.68	0.18	−0.10	0.47	50.0
2	150.2050	1.7360	–	2.929	2.4	4.19	1	2	0.006	44.02	0.04	−0.22	0.30	48.0
2	150.2053	2.5029	–	3.072	3.06	3.09	1	2	0.014	44.07	−0.08	−0.28	0.12	20.0
2	150.2089	2.4819	3.333	3.378	3.37	3.39	1	1	0.024	44.37	−0.49	−0.62	−0.35	0.1
2	150.2090	2.4385	3.715	3.563	3.55	3.57	1	1	0.010	44.09	–	–	−0.717	<0.1
2	150.2108	2.3915	3.095	3.085	3.07	3.1	1	2	0.009	43.88	−0.17	−0.35	0.02	13.0
2	150.2142	2.4750	–	3.075	3.06	3.09	1	2	0.020	44.24	−0.07	−0.17	0.03	20.0
2	150.2146	2.5827	5.3	5.201	5.15	5.28	2	2	0.009	44.42	–	–	0.36	<500.0
2	150.2259	1.7999	–	3.264	3.12	3.46	1	2	0.004	43.63	0.36	0.16	0.55	68.0
2	150.2478	2.4422	3.029	2.992	2.97	3.02	1	2	0.023	44.31	0.10	0.02	0.18	35.0
2	150.2595	2.3761	3.717	2.673	2.66	2.68	1	1	0.008	44.03	–	–	−0.68	<0.1
2	150.2608	2.1180	–	–	>3.0	–	–	–	−0.009	43.97	–	–	–	–
2	150.2618	1.7316	–	3.126	3.08	3.55	2	2	−0.005	43.67	–	–	0.51	>65.0
2	150.2674	1.7009	–	3.412	3.33	3.46	1	1	0.014	44.17	–	–	−0.45	<0.1
2	150.2684	1.7891	–	–	>3.0	–	–	2	0.010	44.02	0.72	0.48	0.87	1000.0
2	150.2716	1.6139	–	3.466	3.44	3.5	2	2	0.011	44.14	0.24	0.0	0.49	60.0
2	150.2848	1.8183	–	–	>3.0	–	–	2	0.011	44.06	−0.033	−0.18	0.25	12.0
2	150.285	2.309	–	2.897	2.42	3.0	2	1	0.011	43.94	−0.38	−0.56	−0.20	1.2
2	150.2881	1.6511	–	3.871	3.13	3.95	1	1	0.018	44.40	–	–	−0.48	<0.1
2	150.2973	2.1489	3.328	3.459	3.45	3.47	1	2	0.005	43.74	−0.11	−0.42	0.20	20.0
2	150.2994	1.6878	–	2.976	2.67	3.14	1	1	0.008	43.83	–	–	−0.24	<9.0
2	150.3007	2.3007	3.498	3.434	3.41	3.46	2	2	0.003	43.55	–	–	0.70	<1000.0
2	150.3048	1.8242	–	2.949	2.49	3.35	1	1	0.006	43.79	–	–	−0.47	<0.1
2	150.3060	1.7616	–	3.265	3.24	3.29	2	2	0.003	43.46	–	–	0.77	<1000.0
2	150.3100	2.5045	–	–	>3.0	–	–	2	0.005	43.75	0.33	0.09	0.48	68.0
2	150.3158	2.3369	–	4.216	3.85	4.44	2	2	0.002	43.47	–	–	0.76	<1000.0
2	150.3179	2.0050	–	3.428	3.38	3.49	2	2	0.007	43.86	–	–	0.03	<30.0
2	150.3187	2.2477	–	–	>3.0	–	–	2	0.008	43.88	0.06	−0.13	0.18	11.0

Table A1 – *continued*

Survey[a]	RA (deg)	Dec. (deg)	z_{spec}	z_{phot}	z_{phot}[b] lower	z_{phot}[c] upper	Optical type[h]	X-ray type[i]	S_{soft}[d]	logLx[e]	HR[f]	HR low[j]	HR up[k]	N_H[g]
2	150.3332	2.4415	–	2.481	2.12	3.07	2	1	0.015	44.09	−0.54	−0.76	−0.33	0.1
2	150.3344	1.7882	–	2.683	2.34	3.02	1	1	0.005	43.60	–	–	−0.24	<8.0
2	150.3443	1.6361	–	3.805	3.74	3.85	2	2	0.019	44.41	–	–	−0.08	<30.0
2	150.3451	1.9579	–	3.065	2.98	3.17	2	2	0.010	43.93	0.18	−0.07	0.25	45.0
2	150.3566	2.2242	–	2.701	2.51	3.09	2	2	−0.008	44.02	–	0.56	–	>75.0
2	150.3598	2.0737	4.917	1.991	1.96	2.01	2	2	0.008	44.30	–	–	0.27	<70.0
2	150.3647	2.1438	3.328	3.361	3.35	3.37	1	1	0.025	44.40	−0.26	−0.38	−0.14	8.0
2	150.3790	1.8761	–	3.33	3.02	3.44	2	2	0.009	43.96	−0.18	−0.44	0.06	14.0
2	150.3809	2.0995	–	4.498	4.43	4.56	2	2	−0.008	44.39	–	0.514	–	>200.0
2	150.3836	2.0748	–	3.852	3.83	3.88	2	2	0.003	43.62	0.40	0.13	0.68	90.0
2	150.3989	2.2709	–	–	>3.0	–	–	2	0.005	43.72	0.46	0.24	0.61	200.0
2	150.4153	1.9342	–	3.681	1.28	3.75	1	1	0.011	44.15	–	–	−0.54	<0.1
2	150.4155	2.3648	–	2.423	2.24	3.29	1	1	0.003	43.47	–	–	−0.29	<6.0
2	150.4251	2.3120	–	3.092	2.98	3.29	2	2	0.003	43.42	0.21	−0.05	0.48	48.0
2	150.4550	1.9674	3.485	3.493	3.46	3.52	1	1	0.007	43.89	–	–	−0.46	<0.1
2	150.4679	2.5315	–	4.45	4.43	4.47	2	1	0.014	44.46	–	–	−0.563	<0.1
2	150.4851	2.4135	–	2.949	2.57	3.51	2	2	−0.006	44.04	–	0.14	–	>25.0
2	150.4862	2.4281	–	3.464	2.95	3.61	2	2	−0.005	43.77	–	0.07	–	32.0
2	150.5467	2.2243	–	3.506	3.35	3.66	2	2	0.029	44.53	−0.08	−0.21	0.03	25.0
2	150.5512	2.1400	–	3.028	2.97	3.07	2	2	−0.024	44.50	–	0.67	–	≥1000.0
2	150.6475	2.4182	–	3.034	2.6	3.32	1	2	−0.052	44.84	–	0.69	–	≥1000.0

[a] 1 = ChaMP; 2 = C-COSMOS.
[b] Photometric redshift lower limit.
[c] Photometric redshift upper limit.
[d] The 0.5–2 keV flux in units of 10^{-13} erg cm^{-2} s^{-1} converted to $\Gamma = 1.8$. For sources undetected in soft band a negative symbol is given and the flux estimated by the hard or full band detection.
[e] The 2–10 keV luminosity in units of erg s^{-1}.
[f] Hardness ratio defined as HR = (H + S)/(H − S), S: 0.5–2.0 keV count rate and H: 2.0–10 keV count rate.
[g] The absorption column density in units of 10^{22}cm^{-2}.
[h] 1: optical type-1 AGNs, and 2: optical type-2 AGNs.
[i] 1: unobscured AGNs, and 2: obscured AGNs; based on $N_H = 10^{22}$ cm^{-2} limit.
[j] HR lower limit.
[k] HR upper limit.

This paper has been typeset from a TEX/LATEX file prepared by the author.